A low-eccentricity migration pathway for a 13-h-period Earth analogue in a four-planet system

nature astronomy

ARTICLES

https://doi.org/10.1038/s41550-022-01641-y

Check for updates

A low-eccentricity migration pathway for a 13-h-period Earth analogue in a four-planet system

Luisa Maria Serrano[1]✉, Davide Gandolfi[1], Alexander J. Mustill[2], Oscar Barragán[3], Judith Korth[4], Fei Dai[5], Seth Redfield[6], Malcolm Fridlund[7,8], Kristine W. F. Lam[9], Matías R. Díaz[10,11], Sascha Grziwa[12], Karen A. Collins[13], John H. Livingston[14], William D. Cochran[15], Coel Hellier[16], Salvatore E. Bellomo[1], Trifon Trifonov[17,18], Florian Rodler[19], Javier Alarcon[19], Jon M. Jenkins[20], David W. Latham[21], George Ricker[22], Sara Seager[22,23,24], Roland Vanderspeck[22], Joshua N. Winn[25], Simon Albrecht[26], Kevin I. Collins[27], Szilárd Csizmadia[28], Tansu Daylan[22], Hans J. Deeg[29,30], Massimiliano Esposito[31], Michael Fausnaugh[22], Iskra Georgieva[7], Elisa Goffo[1,31], Eike Guenther[31], Artie P. Hatzes[31], Steve B. Howell[20], Eric L. N. Jensen[32], Rafael Luque[29,30], Andrew W. Mann[33], Felipe Murgas[29,30], Hannah L. M. Osborne[34], Enric Palle[29,30], Carina M. Persson[7], Pam Rowden[35], Alexander Rudat[22], Alexis M. S. Smith[36], Joseph D. Twicken[20,37], Vincent Van Eylen[34] and Carl Ziegler[38]

It is commonly accepted that exoplanets with orbital periods shorter than one day, also known as ultra-short-period (USP) planets, formed further out within their natal protoplanetary disks before migrating to their current-day orbits via dynamical interactions. One of the most accepted theories suggests a violent scenario involving high-eccentricity migration followed by tidal circularization. Here we present the discovery of a four-planet system orbiting the bright (V = 10.5) K6 dwarf star TOI-500. The innermost planet is a transiting, Earth-sized USP planet with an orbital period of ~13 hours, a mass of $1.42 \pm 0.18\,M_{\oplus}$, a radius of $1.166^{+0.061}_{-0.058}\,R_{\oplus}$ and a mean density of $4.89^{+1.03}_{-0.88}$ g cm^{-3}. Via Doppler spectroscopy, we discovered that the system hosts 3 outer planets on nearly circular orbits with periods of 6.6, 26.2 and 61.3 days and minimum masses of $5.03 \pm 0.41\,M_{\oplus}$, $33.12 \pm 0.88\,M_{\oplus}$ and $15.05^{+1.12}_{-1.11}\,M_{\oplus}$, respectively. The presence of both a USP planet and a low-mass object on a 6.6-day orbit indicates that the architecture of this system can be explained via a scenario in which the planets started on low-eccentricity orbits then moved inwards through a quasi-static secular migration. Our numerical simulations show that this migration channel can bring TOI-500 b to its current location in 2 Gyr, starting from an initial orbit of 0.02 au. TOI-500 is the first four-planet system known to host a USP Earth analogue whose current architecture can be explained via a non-violent migration scenario.

TOI-500 (also known as HIP 34269, TIC 134200185 and CD-47 2804) is a high-proper-motion star (Table 1) with a radial velocity of 55.6 km s^{-1} (ref. [1]) and a V-band magnitude of 10.54 (ref. [2]) located at a distance of 47.39 pc from the Sun[1]. The National Aeronautics and Space Administration's (NASA's) Transiting Exoplanet Survey Satellite[3] (TESS) observed TOI-500 for the first time in sectors 6, 7 and 8 between 11 December 2018 and 28 February 2019. The TESS Science Processing Operations Center[4] (SPOC) identified the signature of a possible Earth-sized transiting planet with an orbital period of nearly 13 hours. The candidate was subsequently designated as TOI-500.01 by the TESS Science Office and announced on 8 March 2019. We performed an independent analysis of the TESS light curves with the codes Détection Spécialisée de Transits[5] and Transit Least Square[6], which confirmed the presence of the candidate (Fig. 1) and excluded additional significant transit signals. We used the Las Cumbres Observatory Global Telescope[7] (LCOGT) to perform photometric observations of the 78 neighbouring stars up to about $\Delta\mathrm{mag} \approx 10$ at angular separation between 12″ and 2.5′ from TOI-500 (Extended Data Fig. 1). The analysis of the retrieved light curves allowed us to exclude that those sources are contaminating eclipsing binaries mimicking the transit signal detected in the TESS light curves. Speckle images acquired with the 4.1 m Southern Astrophysical Research (SOAR) telescope (Cerro Tololo Inter-American Observatory, Chile) and the 8.1 m Gemini South telescope (Cerro Pachón, Chile) excluded the presence of nearby stars up to about $\Delta\mathrm{mag} \approx 7$, as close as 0.02″ (Zorro@Gemini speckle inner working angle; Extended Data Fig. 2) and out to 3″ (SOAR outer limit; Extended Data Fig. 3). Finally, we confirmed the planetary nature of the transit signal with an intensive radial velocity (RV) follow-up campaign carried out with the High-Accuracy Radial Velocity Planet Searcher[8] (HARPS) spectrograph mounted at the 3.6 m telescope of the European Southern Observatory (ESO, La Silla, Chile). We collected nearly 200 HARPS spectra of TOI-500 between 22 March 2019 and 23 March 2020. Our RV measurements also unveiled the presence of three additional Doppler signals that have no counterpart in any of the stellar activity indicators, providing strong evidence that they are induced by three additional planets (Extended Data Figs. 4–6). TOI-500 is thus orbited by (at least) four planets, three of which are not seen to transit their host star. To determine the planetary parameters, we

A full list of affiliations appears at the end of the paper.

Table 1 | TOI-500 main identifiers, equatorial coordinates, parallax, proper motion, optical and infrared magnitudes and fundamental parameters we refer to or we estimated within the present work

	Value	Source[a]
Main identifiers		
TIC 134200185		ExoFOP
CD-47 2804		ExoFOP
HIP 34269		ExoFOP
TYC 8122-00785-1		ExoFOP
2MASS J07061396-4735137		ExoFOP
Gaia DR2 5509620021956148736		Gaia DR2
Equatorial coordinates, parallax and proper motion		
RA (J2000.0)	07 h 06 min 14.18 s	Gaia DR2
Dec. (J2000.0)	−47° 35′ 16.14″	Gaia DR2
Parallax (mas)	21.0715 ± 0.0209	Gaia DR2
μ_α (mas yr^{-1})	135.798 ± 0.040	Gaia DR2
μ_δ (mas yr^{-1})	−146.251 ± 0.037	Gaia DR2
U (km s^{-1})	37.70 ± 0.05	This work
V (km s^{-1})	−60.53 ± 0.19	This work
W (km s^{-1})	6.44 ± 0.06	This work
Optical and near-infrared photometry		
TESS	9.402 ± 0.006	TIC v8
B	11.668 ± 0.050	TIC v8
V	10.540 ± 0.030	TIC v8
J	8.403 ± 0.024	2MASS
H	7.848 ± 0.038	2MASS
K	7.715 ± 0.026	2MASS
W1	7.630 ± 0.030	AllWISE
W2	7.736 ± 0.020	AllWISE
W3	7.658 ± 0.018	AllWISE
W4	7.617 ± 0.124	AllWISE
Fundamental parameters		
$v_\star \sin i_\star$ (km s^{-1})	1.1 ± 0.7	This work
$T_{\rm eff}$ (K)	4,440 ± 100	This work
log($g_\star$) (cgs)	4.618 ± 0.017	This work
[Fe/H]	0.12 ± 0.08	This work
[Ca/H]	−0.01 ± 0.10	This work
$M_\star$ ($M_\odot$)	0.740 ± 0.017	This work
$R_\star$ ($R_\odot$)	0.678 ± 0.016	This work
Age (Gyr)	5.0 ± 0.2	This work
Distance (pc)	47.3924 ± 0.0473	Gaia DR2
A_v	0.02 ± 0.02	This work

[a]Exoplanet Follow-up Observing Program (ExoFOP) database; Gaia Data Release 2 (DR2; ref. [1]); TESS Input Catalog version 8 (TIC v8; ref. [119]); Two Micron All Sky Survey (2MASS; ref. [74]) catalogue; Wide-field Infrared Survey Explorer (AllWISE; ref. [120]) data release. μ_α and μ_δ are the components of the stellar proper motion.

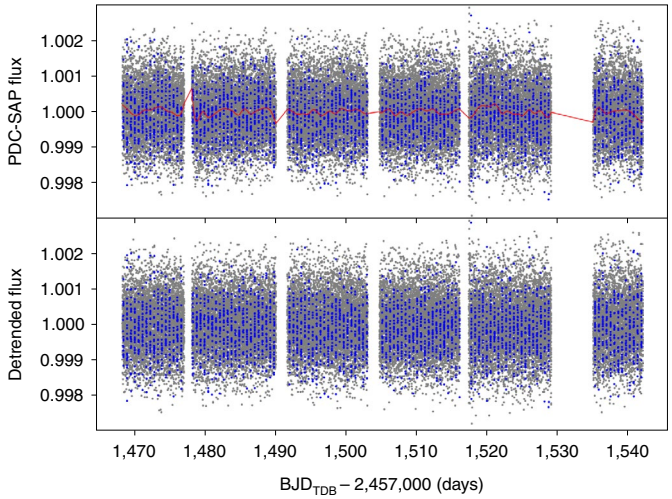

Fig. 1 | TOI-500 TESS photometric data. Upper panel: median-normalized PDC-SAP TESS light curve of TOI-500 (grey points). The spline used to detrend the TESS data is overplotted with a red line. Lower panel: detrended light curve following the removal of outliers using a sigma clipping algorithm. The light curve was detrended following method 3 as described in the 'Independent transit search' section in the Methods. The data points within the transits of TOI-500 b are plotted with blue circles in both panels.

simultaneously modelled the transit photometry and radial velocity measurements using the software pyaneti[9] (Figs. 2 and 3). We also derived the fundamental parameters of the host star by analysing the co-added HARPS spectrum with the code Spectroscopy Made Easy[10,11] (SME). We inferred the stellar mass, radius and age using the Bayesian web-tool PARAM 1.3 (ref. [12]). To measure the rotational period of the star, we performed a frequency analysis of the existing Wide Angle Search for Planets[13] (WASP-South) ground-based photometry (Extended Data Fig. 7) and frequency (Extended Data Fig. 6) and Bayesian (Extended Data Fig. 8) analyses of the HARPS activity indicators.

TOI-500 b has an orbital period of $P_{\rm b} = 0.548177 \pm 0.000019$ days. Its mass of $M_{\rm b} = 1.42 \pm 0.18\,M_\oplus$ and radius of $R_{\rm b} = 1.166^{+0.061}_{-0.058}\,R_\oplus$ imply a mean density of $\rho_{\rm b} = 4.89^{+1.03}_{-0.88}$ g cm^{-3}. For the other three planets, we could only measure their minimum masses because, in the absence of transit detection, the inclinations of their orbits remain unknown. TOI-500 c, d and e have periods of $P_{\rm c} = 6.6356 \pm 0.0040$ days, $P_{\rm d} = 26.233 \pm 0.020$ days and $P_{\rm e} = 61.30 \pm 0.28$ days and minimum masses of $M_{\rm c}\sin i_{\rm c} = 5.03 \pm 0.41\,M_\oplus$, $M_{\rm d}\sin i_{\rm d} = 33.12 \pm 0.88\,M_\oplus$ and $M_{\rm e}\sin i_{\rm e} = 15.05^{+1.12}_{-1.11}\,M_\oplus$, respectively (Table 2). The four planets have nearly circular orbits, with eccentricities comparable with zero within 1.5σ. The host star TOI-500 is a K6 dwarf with a mass of $M_\star = 0.740 \pm 0.017\,M_\odot$, a radius of $R_\star = 0.678 \pm 0.016\,R_\odot$ and iron and calcium abundances of [Fe/H] = 0.12 ± 0.08 and [Ca/H] = −0.01 ± 0.10, respectively. The interstellar extinction along the line of sight is consistent with zero, being $A_v = 0.02 \pm 0.02$. The rotational period of the star is $P_{\rm rot} = 43.73^{+0.21}_{-0.20}$ days, in agreement with previous results by ref. [14], while the isochronal and gyrochronological ages are 4.7 ± 4.0 Gyr and 5.0 ± 0.2 Gyr, respectively. The fundamental parameters of TOI-500 are listed in Table 1.

According to its physical properties, TOI-500 b is a new member of a very small sample of Earth analogues with well-known masses and radii. More importantly, it is the USP planet with the lowest mass and smallest radius known so far within the sample of ultra-short-period planets belonging to multi-planet systems. Figure 4 shows the mass–radius diagram for USP planets with radii between 1 and 2 $R_\oplus$ and masses <10 $M_\oplus$. Most of the USP small planets (for example, Kepler-78 b[15] and CoRoT-7 b[16]) have a bulk composition comprising ~30% iron and ~70% silicates[17], similar to Earth. Although TOI-500 b falls in this same interval of compositions, it stands out of the crowd because, after GJ 367 b[18], it is the leftmost planet in the plot, one of the smallest and lightest of its type.

Like most of the small USP planets, TOI-500 b is expected to be a lava-ocean planet[16], because the close vicinity to its host star

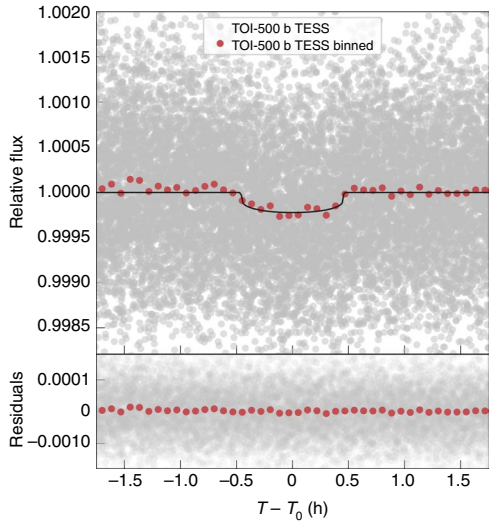

Fig. 2 | TOI-500 b phase-folded transit. Upper panel: phase-folded TESS light curve of TOI-500 b. TESS measurements are shown with light grey circles, along with the 5 min binned data (red circles) and the inferred transit model (solid black line). Lower panel: residuals to the fit. T-T0 within the *x*-axis label stands for time from mid-transit time.

renders the surface extremely hot. Assuming the planet is a black body with zero albedo, we estimated an equilibrium temperature of $T_{eq} = 1{,}617 \pm 41$ K. As such, it is likely that TOI-500 b does not have a primary atmosphere inherited from the formation process and has undergone complete photo-evaporation during the formation and evolution processes[17]. The extreme vicinity to the host star could also have caused the formation of a metallic (secondary) atmosphere, possibly via volcanic out-gassing, as might have happened on 55 Cancri e (see ref. [19] for the estimated upper limit of atmospheric composition, and also ref. [20]) and for planet Earth. A statistical analysis of the atmospheric predicted signal-to-noise (S/N) ratio of Earth-sized planets thus-far discovered showed that TOI-500 b stands among the top 10 objects, meaning it is a promising target to perform atmospheric studies with current and future instruments (Methods and Extended Data Fig. 9).

Based on their minimum masses, TOI-500 c is probably a super-Earth, while TOI-500 d and e are more likely to be Neptunian planets[21]. Although the 3 outer planets do not transit their host star, a co-planar geometry of the system is not excluded as this would imply an impact parameter >2 for planets c, d and e, accounting for the null detection of their transits. Dynamical simulations carried out with rebound[22] and reboundx[23] and covering 10^8 orbits of the USP planet ruled out orbits with high mutual inclination. We constrained the orbital inclination for the outer two planets TOI-500 d and e to lie between 40° and 90°, and ruled out an inclination $i_c < 30°$ for planet c.

Ultra-short-period planets most likely did not form at their current locations, as these are often in close-in orbits within the dust sublimation radius of the proto-stellar disk[24]. Dynamical interactions could lead close-in super-Earths to reach high eccentricities and circularize to orbits with $P < 1$ day (ref. [25]). The inward migration of USP planets is also evident through their larger orbital period ratios and larger mutual inclination, compared with longer period planets belonging to the same system[26,27]. How this migration occurred is still debated[28–31]. The secular formation scenario[29–31] suggests that the presence of several close-in planetary companions provides the dynamical interaction necessary for the migration to occur. Moreover, it requires that the outer planets have enough angular momentum deficit (see equation 4 in ref. [32]) to launch the USP planet into an eccentric inward-migrating orbit. TOI-500 provides us with a unique opportunity to compare the predictions of different secular formation scenarios.

The bright and not very active host star allowed us to map out the inner planetary architecture of the system with hundreds of RV data points over a baseline of one year. We found that the orbital period ratio between planets b and c is about 12, while within most Kepler planetary systems the 2 close-in planets have a period ratio lower than 4 (ref. [33]). This higher period ratio is the hallmark of the inward migration commonly seen in other systems known to host USP planets (Fig. 5). Furthermore, since the ratios of the orbital periods of the non-transiting planets are not in a first or second order but in 1:4 (P_c and P_d) and 3:7 (P_d and P_e) commensurabilities, secular forces dominate the dynamical interaction between the planets.

One of the migration models for USP planets, described in ref. [30] and mentioned in ref. [29], involves the excitation of the eccentricities to high values, leading to the formation of USP planets in highly mutually inclined orbits with respect to the outer planetary companions (>30°; see ref. [30] for an in-depth description of the model). While eccentricities are quickly damped out by tidal dissipation inside the planet on kyr-to-Myr timescales[17], orbital inclinations are only damped by dissipation inside the host star and persist over Gyr (ref. [17]). Indeed, many USPs are observed on orbits with high mutual inclinations[27,34] and our system easily accommodates itself in this model. Assuming that the USP planet TOI-500 b emerged from the protoplanetary disk, before tidal migration, at an initial orbit of about 3 days (safely beyond the dust sublimation radius and Hill radius instability from planet c), we estimated that the minimum angular momentum deficit for it to undergo inward migration can be achieved as long as the outer planets currently have either eccentricities of ~0.05 or mutual inclinations of ~4° (ref. [29]), conditions that are well fitted by TOI-500.

The sample of USP planets is so small that whenever we discover a new one it is important to explore which other existing migration processes might explain the final architecture. Ref. [29] has described several scenarios that can justify some rare planetary system configurations involving a USP planet. One of them is the low-eccentricity channel, according to which the USP planet and its companions emerge from the protoplanetary disk with relatively low orbital eccentricities, small semi-major axes and low orbital inclinations. The eccentricities, damped by tidal forces, slowly decay towards zero in a quasi-equilibrium state, while the semi-major axes decay much more slowly than in the high-eccentricity case. In addition, since the secular behaviour remains linear, the inclination fluctuations remain small, without the large chaotic variations expected in the high-eccentricity channel. After billions of years, the system stabilizes itself with almost zero eccentricities and co-planar orbits, and it will have one small USP planet and at least one additional companion, usually a super-Earth, with an orbital period shorter than ~10 days. The current architecture of TOI-500 fits well within these conditions, implying that the four planets might have undergone the low-eccentricity scenario before fully stabilizing. With a view to provide evidence for (or against) this scenario, we performed simulations in which we tested the evolution of TOI-500 over the course of 5 Gyr, starting from a set of initial conditions as listed: semi-major axis a_b between 0.02 and 0.03 au, initial eccentricities e_b and $e_c = 0.05$ and e_d and $e_e \in \{0.05, 0.1, 0.15, 0.2, 0.25\}$. When the system reached the observed configuration, the integration would stop. We found that the low-eccentricity migration channel can bring TOI-500 b to its current location in 2 Gyr, from an initial orbit of just beyond 0.02 au, as long as the outer planets' eccentricities are not too low (Methods and Fig. 6).

Thanks to the extensive RV follow-up with HARPS, TOI-500 is the first multi-planetary system with precise mass measurements comprising a small USP planet and more than one non-Jupiter-type

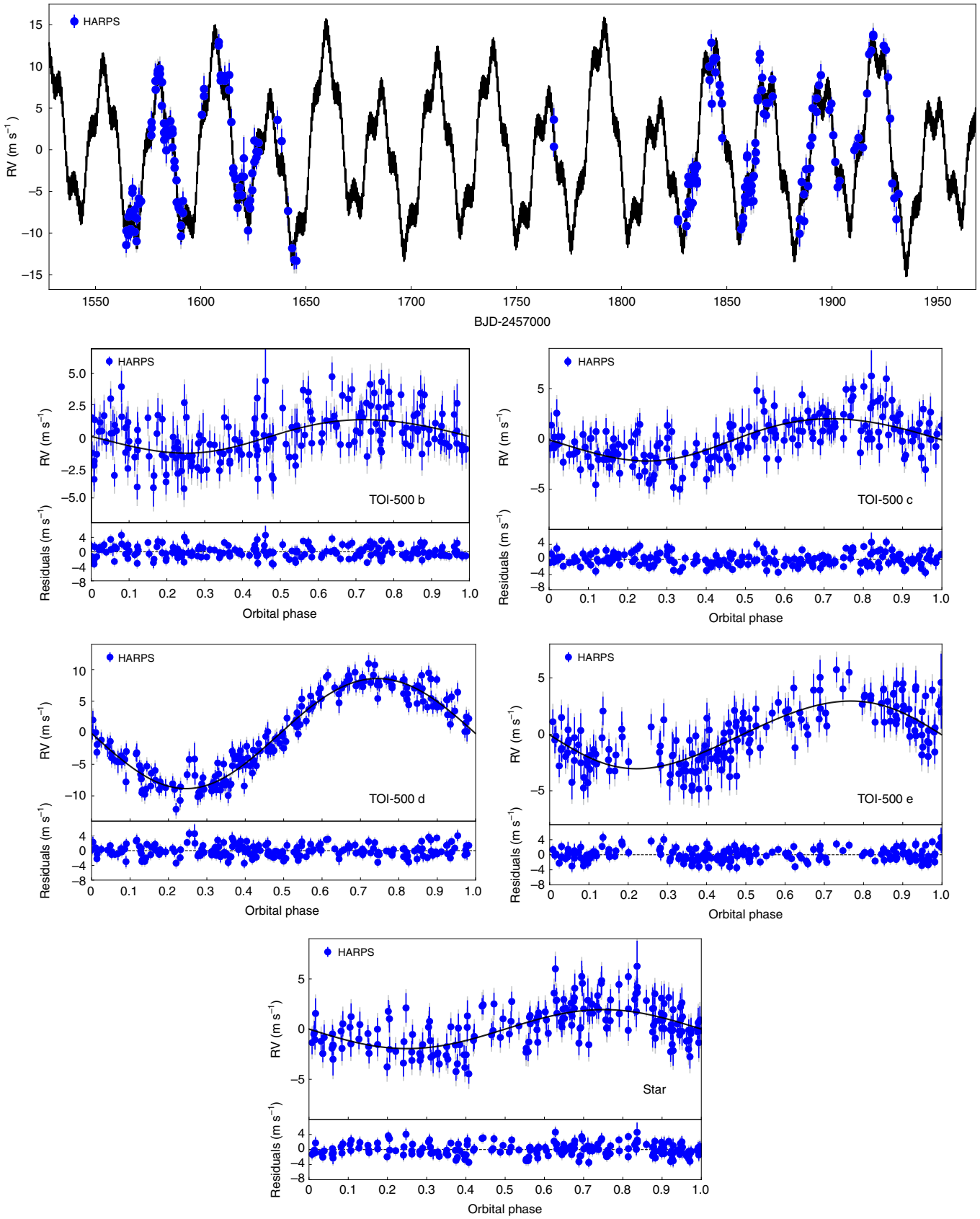

Fig. 3 | HARPS RV best fit. First row: HARPS SERVAL RVs (blue data points) and best-fitting five-signal model (black line; four planets plus stellar rotation). Second, third and fourth rows: phase-folded RVs curve of TOI-500 b (second row, left panel), TOI-500 c (second row, right panel), TOI-500 d (third row, left panel), TOI-500 e (third row, right panel) and stellar rotation (fourth row).

Table 2 | TOI-500 system parameters as derived from the joint modelling of the TESS and HARPS data

Parameter	Prior[a]	Results with GP stellar model	Results with stellar sinusoidal model
Model parameters for TOI-500 b			
Orbital period P_b (d)	$\mathcal{U}[0.5478,\ 0.5485]$	0.548172 ± 0.000019	0.548177 ± 0.000019
Transit epoch $T_{0,b}$ ($BJD_{TDB} - 2{,}457{,}000$)	$\mathcal{U}[1,468.3660,\ 1,468.4140]$	$1{,}468.3909 \pm 0.0017$	$1{,}468.3905 \pm 0.0017$
$\sqrt{e_b}\sin\omega_{\star,b}$	$\mathcal{U}[-1,\ 1]$	$-0.03^{+0.21}_{-0.23}$	-0.07 ± 0.24
$\sqrt{e_b}\cos\omega_{\star,b}$	$\mathcal{U}[-1,\ 1]$	$-0.09^{+0.19}_{-0.16}$	0.02 ± 0.17
Scaled planetary radius $R_b/R_\star$	$\mathcal{U}[0,\ 0.022]$	0.01568 ± 0.00068	$0.01577^{+0.00072}_{-0.00070}$
Impact parameter, b_b	$\mathcal{U}[0,\ 1]$	$0.51^{+0.12}_{-0.17}$	$0.53^{+0.12}_{-0.18}$
Radial velocity semi-amplitude variation K_b (ms^{-1})	$\mathcal{U}[0,\ 4]$	1.56 ± 0.20	1.35 ± 0.17
Model parameters for TOI-500 c			
Orbital period P_c (d)	$\mathcal{U}[6.5857,\ 6.6857]$	6.6299 ± 0.0051	6.6356 ± 0.0040
Time of inferior conjunction $T_{0,c}$ ($BJD_{TDB} - 2{,}457{,}000$)	$\mathcal{U}[1,559.7073,\ 1,564.1311]$	$1{,}562.09 \pm 0.20$	$1{,}561.96 \pm 0.20$
$\sqrt{e_c}\sin\omega_{\star,c}$	$\mathcal{U}[-1,\ 1]$	-0.03 ± 0.23	-0.04 ± 0.20
$\sqrt{e_c}\cos\omega_{\star,c}$	$\mathcal{U}[-1,\ 1]$	$0.22^{+0.19}_{-0.27}$	$0.11^{+0.19}_{-0.22}$
Radial velocity semi-amplitude variation K_c (ms^{-1})	$\mathcal{U}[0,\ 4.5]$	1.95 ± 0.21	2.10 ± 0.17
Model parameters for TOI-500 d			
Orbital period P_d (d)	$\mathcal{U}[25.4334,\ 27.0334]$	26.235 ± 0.024	26.233 ± 0.020
Time of inferior conjunction $T_{0,d}$ ($BJD_{TDB} - 2{,}457{,}000$)	$\mathcal{U}[1,578.4891,\ 1,595.9780]$	$1{,}587.20 \pm 0.24$	$1{,}587.22^{+0.22}_{-0.20}$
$\sqrt{e_d}\sin\omega_{\star,d}$	$\mathcal{U}[-1,\ 1]$	0.04 ± 0.11	$-0.011^{+0.101}_{-0.099}$
$\sqrt{e_d}\cos\omega_{\star,d}$	$\mathcal{U}[-1,\ 1]$	0.04 ± 0.11	$-0.045^{+0.104}_{-0.091}$
Radial velocity semi-amplitude variation K_d (ms^{-1})	$\mathcal{U}[0,\ 15]$	$8.83^{+0.25}_{-0.23}$	8.72 ± 0.19
Model parameters for TOI-500 e			
Orbital period P_e (d)	$\mathcal{U}[58.1620,\ 64.1620]$	$60.33^{+0.32}_{-0.33}$	61.30 ± 0.28
Time of inferior conjunction $T_{0,e}$ ($BJD_{TDB} - 2{,}457{,}000$)	$\mathcal{U}[1,834.4801,\ 1,895.6421]$	…	$1{,}865.82^{+1.16}_{-1.32}$
Time of inferior conjunction $T_{0,e}$ ($BJD_{TDB} - 2{,}457{,}000$)	$\mathcal{N}[1,865.8,\ 3]$	$1{,}865.22^{+0.91}_{-1.03}$	…
$\sqrt{e_e}\sin\omega_{\star,e}$	$\mathcal{U}[-1,\ 1]$	$0.12^{+0.19}_{-0.22}$	$0.04^{+0.18}_{-0.19}$
$\sqrt{e_e}\cos\omega_{\star,e}$	$\mathcal{U}[-1,\ 1]$	$0.21^{+0.15}_{-0.20}$	$0.18^{+0.14}_{-0.20}$
Radial velocity semi-amplitude variation K_e (ms^{-1})	$\mathcal{U}[0,\ 10]$	2.40 ± 0.27	3.00 ± 0.22
Model parameters of activity-induced RV signal			
Period $P_\star$ (d)	$\mathcal{U}[41.6940,\ 45.6940]$	…	$43.73^{+0.21}_{-0.20}$
Epoch $T_{0,\star}$ ($BJD - 2{,}457{,}000$)	$\mathcal{U}[1,562.1299,\ 1,605.8239]$	…	$1{,}583.92^{+1.10}_{-1.11}$
Radial velocity semi-amplitude variation $K_\star$ (ms^{-1})	$\mathcal{U}[0,\ 4]$	…	1.94 ± 0.20
Multi-dimensional GP parameters			
GP period P_{GP} (d)	$\mathcal{U}[35,\ 50]$	$44.57^{+2.05}_{-2.94}$	…
λ_p	$\mathcal{J}[0.1,\ 10]$	$2.70^{+4.33}_{-1.52}$	…
λ_e (d)	$\mathcal{J}[50,\ 250]$	$105.0^{+93.8}_{-50.2}$	…
V_c ($m\,s^{-1}$)	$\mathcal{U}[0,\ 1]$	$5.6^{+30.1}_{-4.1}$	…
V_r ($m\,s^{-1}\,d^{-1}$)	$\mathcal{U}[-1,\ 1]$	3^{+32}_{-19}	…
F_c ($km\,s^{-1}$)	$\mathcal{U}[-1,\ 1]$	$0.21^{+1.03}_{-0.15}$	…
S_c	$\mathcal{U}[-1,\ 1]$	$0.057^{+0.284}_{-0.041}$	…
Other system parameters			
Stellar density $\rho_\star$ ($g\,cm^{-3}$)	$\mathcal{N}[3.34,\ 0.25]$	$3.38^{+0.26}_{-0.24}$	$3.37^{+0.25}_{-0.23}$

Continued

Table 2 | TOI-500 system parameters as derived from the joint modelling of the TESS and HARPS data (Continued)

Parameter	Prior[a]	Results with GP stellar model	Results with stellar sinusoidal model
RV jitter term σ_{HARPS} (ms^{-1})	$\mathcal{U}[1.041, 1.230]$	1.50 ± 0.21	1.16 ± 0.12
Parameterized limb-darkening coefficient q_1	$\mathcal{N}[0.45, 0.10]$	$0.484^{+0.100}_{-0.093}$	$0.483^{+0.098}_{-0.096}$
Parameterized limb-darkening coefficient q_2	$\mathcal{N}[0.38, 0.10]$	$0.399^{+0.103}_{-0.099}$	0.404 ± 0.098
Derived parameters for TOI-500 b			
Planet mass M_b ($M_\oplus$)	···	1.64 ± 0.21	1.42 ± 0.18
Planet radius R_b ($R_\oplus$)	···	1.159 ± 0.058	$1.166^{+0.061}_{-0.058}$
Planet density ρ_b ($g\,cm^{-3}$)	···	$5.78^{+1.23}_{-1.04}$	$4.89^{+1.03}_{-0.88}$
Scaled semi-major axis, $a_b/R_\star$	···	3.769 ± 0.090	3.769 ± 0.090
Semi-major axis a_b (au)	···	0.01188 ± 0.00040	$0.01189^{+0.00041}_{-0.00040}$
Orbital inclination i_b (deg)	···	$82.31^{+2.35}_{-1.41}$	$82.09^{+2.53}_{-1.31}$
e_b	···	$0.063^{+0.068}_{-0.044}$	$0.063^{+0.073}_{-0.044}$
$\omega_{\star,b}$ (deg)	···	$316.2^{+181.7}_{-95.9}$	$228.5^{+72.9}_{-160.6}$
Transit duration $T_{dur,b}$ (h)	···	$1.002^{+0.051}_{-0.045}$	$0.998^{+0.050}_{-0.044}$
Transit depth $T_{depth,b}$ (ppm)	···	$245.9^{+21.8}_{-20.8}$	$248.7^{22.6}_{22.0}$
Equilibrium temperature $T_{eq,b}$ (K)	···	$1,617 \pm 41$	$1,617 \pm 41$
Insolation F_b ($F_\oplus$)	···	$1,140^{+121}_{-112}$	$1,138^{+123}_{-112}$
Derived parameters for the other planets			
$M_c \sin i_c$ ($M_\oplus$)	···	4.64 ± 0.50	5.03 ± 0.41
e_c	···	$0.111^{+0.102}_{-0.076}$	$0.072^{+0.074}_{-0.050}$
$\omega_{\star,c}$ (deg)	···	$352.4^{+54.4}_{-76.2}$	$228.0^{+100.0}_{-197.0}$
$M_d \sin i_d$ ($M_\oplus$)	···	$33.54^{+1.07}_{-1.02}$	33.12 ± 0.88
e_d	···	$0.019^{+0.020}_{-0.013}$	$0.016^{+0.017}_{-0.011}$
$\omega_{\star,d}$ (deg)	···	$27.2^{+81.9}_{-104.8}$	$189.6^{+92.3}_{-93.3}$
$M_e \sin i_e$ ($M_\oplus$)	···	$11.94^{+1.36}_{-1.34}$	$15.05^{+1.12}_{-1.11}$
e_e	···	$0.106^{+0.092}_{-0.075}$	$0.073^{+0.068}_{-0.051}$
$\omega_{\star,e}$ (deg)	···	$28.1^{+43.6}_{-60.9}$	$103.7^{+228.2}_{-80.7}$
Other derived parameters			
Limb darkening u_1	···	$0.55^{+0.16}_{-0.15}$	$0.55^{+0.15}_{-0.14}$
Limb darkening u_2	···	$0.14^{+0.14}_{-0.14}$	$0.13^{+0.14}_{-0.13}$

[a]$\mathcal{U}$, $\mathcal{N}$ and $\mathcal{J}$ refer to uniform, Gaussian and Jeffreys priors, respectively. Note: $\omega_\star$ stands for stellar periastron argument.

companion for which the low-eccentricity scenario has been demonstrated to predict the planetary final architecture. We emphasize that this has been done without the use of any additional assumptions. Prior to our work, ref. [30] could apply a low-eccentricity scenario on Kepler-10 and Kepler-290, but in the first case they needed to add another Earth-like object between planets b and c, while in the second case they assumed values for the planetary masses. TOI-500 is not the only existing system for which the low-eccentricity channel may work. For instance, TOI-561[35] and CoRoT-7[16,36] could also have migrated with the same scenario. CoRoT-7 is a two-planet system with no analogues thus far: an active star with a USP planet and a 3-day-period Neptune. Testing the model on this system might be interesting, because it could allow predictions about the debated third planet, CoRoT-7 d[37–39]. TOI-561 is, on the contrary, very similar to TOI-500, although planet c has a period of 11.77 days. It could therefore be a good laboratory to test whether the theory can work, given that the orbital period of the second planet is longer than the 10-day requirement mentioned in ref. [29].

The presence of the smallest and lightest USP planet known to belong to a multi-planetary system, the close commensurability of the three outer planets, and the additional discovery of a planet with period shorter than 10 days makes TOI-500 extremely compelling and rare. The compatibility of the system with a less common secular scenario of migration discloses a new path of future exploration aiming at identifying other cases in which the low-eccentricity scenario can account for the current location of USP planets. The possibility that TOI-500 b might have a secondary atmosphere makes this system an important laboratory for future atmospheric analysis with, for example, the Echelle SPectrograph for Rocky Exoplanets and Stable Spectroscopic Observations (ESPRESSO), the EXtreme PREcision Spectrometer (EXPRES) and the James Webb Space Telescope.

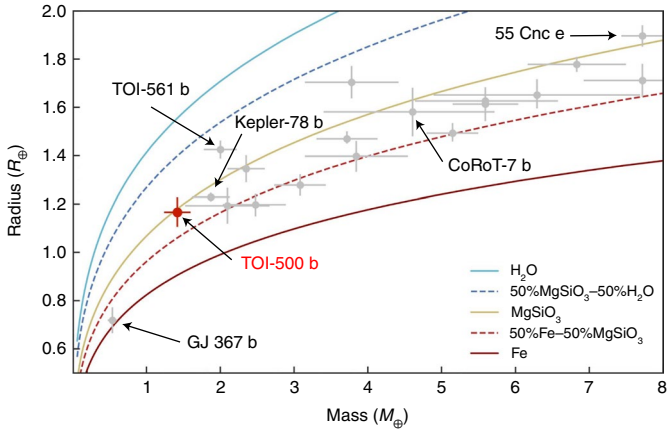

Fig. 4 | Mass–radius diagram for USP planets. All planets have period $P<1$ d and mass and radius known with precision >30% as retrieved from the Transiting Extrasolar Planet Catalogue[121] (TEPCat) (grey dots). The position of TOI-500 b is highlighted with a red dot. The thick and dashed lines mark the bulk composition models extrapolated from ref. [122] and explained in the caption of the figure. Each planet is reported with horizontal and vertical error-bars which correspond to the 3σ uncertainties on the radius and on the mass.

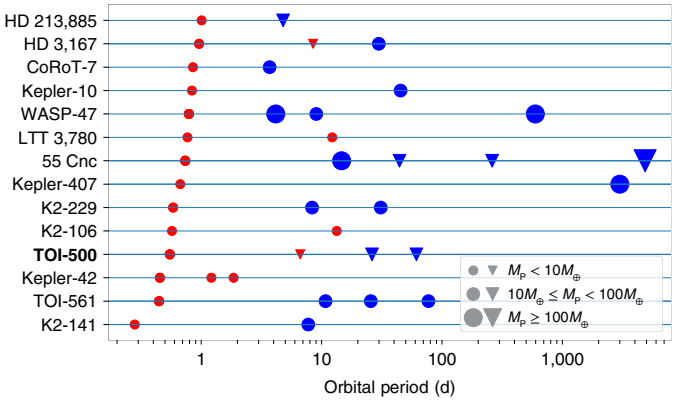

Fig. 5 | Multi-planetary systems hosting a USP planet whose mass and radius are known as of December 2021. From top to bottom, systems are sorted by decreasing period of their USP planet. The *x* axis displays the orbital period in logarithmic scale. The size of the symbols depends on the mass of the planet (M_p): we used the smallest symbols for planets with masses lower than 10 $M_\oplus$, the medium-size symbols for planets with masses between 10 $M_\oplus$ and 100 $M_\oplus$ and the largest symbol for masses above 100 $M_\oplus$. We highlighted in red the Earth-like planets, while the gaseous planets are in blue. The planets with measured mass and radius are marked with dots, while those with only the radius or the minimum mass known are marked with triangles. For non-transiting planets, we assumed that the planetary mass is the minimum mass. For transiting planets with no RV measurements, we used equation (1) in ref. [21] to estimate the planetary mass. The systems were identified by cross-matching the the Extrasolar Planets Encyclopedia (https://exoplanet.eu) and TEPCat (https://www.astro.keele.ac.uk/jkt/tepcat/; ref. [123]). Planetary parameters are extracted from refs. [94,124] for K2-141, ref. [35] for TOI-561, refs. [125,126] for Kepler-42, refs. [127–130] for K2-106, refs. [129,131] for K2-229, ref. [132] for Kepler-407, refs. [133–138] for 55 Cnc, refs. [139,140] for LTT 3780, refs. [141–146] for WASP-47, ref. [33] for Kepler-32, refs. [147–152] for Kepler-10, refs. [16,36–39,93,153] for CoRoT-7, refs. [63,154,155] for HD 3167 and ref. [156] for HD 213885 (also known as TOI-141). TOI-500 is highlighted in boldface.

Methods

Transit search. *TESS observations.* TESS observed TOI-500 in cycle 1 during three consecutive sectors (namely, sectors 6, 7 and 8), between 11 December 2018 and 28 February 2019. The star was photometrically monitored every 2 minutes by TESS camera #3 using the Charged Couple Device (CCD) #4 for the first two sectors, and CCD #3 for sector 8. The data from each sector have a gap of about 0.98 d, due to the data downlink at the satellite perigee passage. The sector 8 light curve shows an additional 1-day gap due to an instrument failure that occurred on 14 February 2019 (Fig. 1).

We retrieved the TESS light curves of TOI-500 from the Mikulski Archive for Space Telescope (https://mast.stsci.edu). The data products were extracted by SPOC[4] at NASA Ames Research Center and include simple-aperture photometry (SAP) and the so-called PDC-SAP, a systematics-corrected photometry obtained by applying to the SAP time series the presearch data conditioning algorithm (PDC) developed for Kepler light curves[40–42]. SPOC conducted with its pipeline multiple transiting-planet searches, which stop when the significance of a transit signal is below a given detection threshold. They produced the data validation report for the combined sector 6–8 datasets[43,44] and published it on 4 May 2019.

The vetting team at Massachusetts Institute of Technology (MIT) reviewed the threshold crossing events within the data validation report of TOI-500 and announced the detection of a transiting signal with a period of $P_{orb}\approx0.55$ d, a depth of about 230 ppm and a duration of $T_{14}\approx1.0$ hour. The transiting-planet candidate passed all the validation tests from the threshold crossing events, such as odd–even transit depth variation and ghost diagnostic tests, which helped to rule out an eclipsing-binary scenario.

LCOGT observations. We observed TOI-500 continuously for 190 min in the Sloan r′ band on 3 March 2019 and again for 156 min on 2 May 2019 in the Panoramic Survey Telescope and Rapid Response System (Pan-STARRS) z-short band from the LCOGT[7] 1-m network nodes at South Africa Astronomical Observatory and at Cerro Tololo Inter-American Observatory, respectively. The 4,096 × 4,096 LCOGT Sinistro cameras have an image scale of 0.389″ per pixel, resulting in a 26′ × 26′ field of view. The images were calibrated by the standard LCOGT BANZAI pipeline[45], and photometric data were extracted with AstroImageJ[46]. Using the TOI-500 b ephemeris from the TESS sector 7 SPOC data validation report to predict transit timing, each of our observations covered full-transit-duration windows, and the combined transits provided 75 min of phase coverage before and after transit. The SPOC pipeline transit depth of 231 ppm is generally too shallow to be reliably detected with ground-based observations, so we intentionally saturated TOI-500 to check for possible near eclipsing binaries (NEBs) that could be contaminating the TESS photometric aperture that generally extends ~1′ from the target star. To account for possible contamination from the wings of neighbouring star point-spread functions, we searched for NEBs out to 2.5′ from the target star. We placed apertures according to Gaia DR2 positions and proper motion. If fully blended in the SPOC aperture, a neighbouring star that is fainter than the target star by 9.1 magnitudes in TESS band could produce the SPOC-reported flux deficit at mid-transit (assuming a 100% eclipse). To account for possible Δmag differences between TESS band and the follow-up bands, we included an extra 0.5 magnitudes fainter (down to TESS-band magnitude 19, that is, Δmag ≈ 10). Our search ruled out NEBs in all 78 neighbouring stars that met our search criteria (Extended Data Fig. 1). All the searched stars had a minimum distance from TOI-500 of 12″. We detected no additional source at smaller distances, excluding any blending induced on TOI-500 by a contamination source.

Super-WASP observations. The field of TOI-500 was observed with WASP-South[13] over 4 consecutive years from 2008 to 2012, in each year with observing spans of 170 nights from October to March. Nearly 26,000 photometric data points were obtained, with a typical cadence on clear nights of 15 min. WASP-South was then equipped with 200 mm, f/1.8 lenses backed by 2,048 × 2,048 CCDs and observed with a 400–700 nm filter[13]. TOI-500 is 4 magnitudes brighter than any other star in the 48″ photometric extraction aperture. No sign of a transiting planet was found in Super-WASP observations due to the high impact of the instrumental noise on the data, bound to mask the shallow transits of the planets.

We searched the data for a rotational modulation using a periodogram analysis[47]. The light curve from the 2008/2009 season shows a possible periodicity near 0.022 d^{-1}, corresponding to a period of about 45 d, with an amplitude of 2 mmag and an estimated false-alarm probability of 1%. This is not seen in the following two years. The ~45 d period is possibly seen again in 2011/2012, once more with an amplitude of 2 mmag and a false-alarm probability near 1% (Extended Data Fig. 7). Combining all 4 years of data again produces a peak at a period of 45 ± 5 d (where the error allows for the modulation being incoherent), with a 1% false-alarm probability and an amplitude of 1 mmag.

High-resolution imaging. Sources that are not detected in seeing-limited photometry or by Gaia can lead to photometric contamination of the TESS light curve of TOI-500. Dilution of the transit depth can lead to an underestimated planet radius or can make astrophysical false positives appear planetary in nature[48]. We thus searched for nearby stellar companions using 4- and 8-m class telescopes, providing robust limits on the presence of companions and the level of photometric dilution.

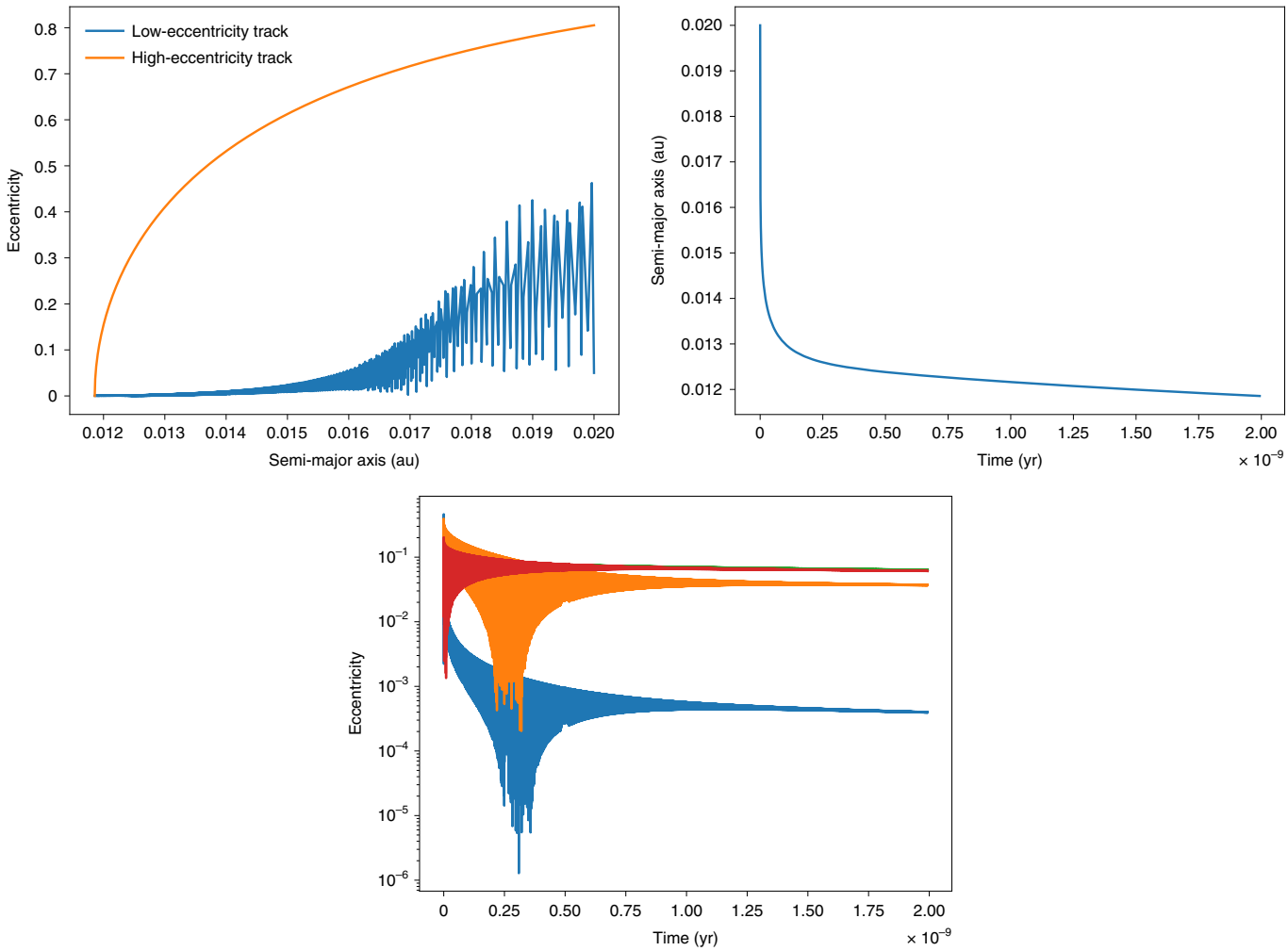

Fig. 6 | Example migration of TOI-500 b from 0.02 au to its current orbit. Top left panel: the blue curve shows the evolution of semi-major axis and eccentricity in a low-eccentricity pathway with initial eccentricities $e_b = 0.05$, $e_c = 0.05$, $e_d = 0.05$ and $e_e = 0.2$. By contrast, the orange curve shows an analytical high-eccentricity migration track, where the planet rapidly circularizes from a highly eccentric orbit while conserving its orbital angular momentum. Top right panel: the semi-major axis evolution of the USP in this system. Bottom panel: the eccentricity evolution of all planets in this system (USP in blue).

Lucky imaging with Gemini/Zorro. On 16 March 2020, TOI-500 was observed using the Zorro speckle imager[49], mounted on the 8.1 m Gemini South telescope in Cerro Pachón, Chile. Zorro uses high speed electron-multiplying CCDs to simultaneously acquire data in two bands centred at 562 nm and 832 nm. The data were collected and reduced following the procedures described in ref. [50]. The resulting reconstructed image achieved a contrast of Δmag = 7.4 at a separation of 1″ in the 832 nm band, without showing any contamination resource (bottom panel of Extended Data Fig. 2).

High contrast imaging with SOAR/HRCam. On 18 May 2019, TOI-500 was observed in the I band with a pixel scale of 0.01575″ pix^{-1} using the HRCam imager, mounted on the 4.1 m SOAR telescope at Cerro Tololo Inter-American Observatory, Chile. The data were acquired and reduced following the procedures described in refs. [51] and [52]. The resulting reconstructed image achieved a contrast of Δmag = 7.2 at a separation of 3″ (top panel of Extended Data Fig. 3). The Zorro inner working angles of 17 and 28 mas (at 562 nm and 832 nm, respectively) yield spatial limits at the star of ~1 au (for distance $d = 47$ pc of the star from our Solar System), near the orbital period semi-major axis of the outer planets. Any source within the speckle spatial limits cannot be a massive star because we would have detected it. A similar companion would have been disrupted long ago. Theoretical studies have shown that a close companion can truncate protoplanetary disks and newly forming planets[53,54] or disperse the disk before planets even begin to form[55,56]. The obtained image contrast eliminates all other possible companions outside the inner working angle down to ~M5V and out to a distance of ~56 au (at 1.2″).

HARPS RV observations. We observed TOI-500 with the HARPS[8] spectrograph mounted at the ESO 3.6-m telescope of La Silla Observatory, Chile. Between 22 March 2019 and 23 March 2020, we collected 197 high-resolution spectra with a resolving power of $R = \lambda/\Delta\lambda \approx 115{,}000$, as part of the observing programmes 1102.C-0923, 0103.C-0874 and 60.A-9709. We monitored the sky background using the second fibre of the instrument and set the exposure time to 900–2,100 s, depending on sky conditions and constraints of the observing schedule. Given the relatively short orbital period of the transiting candidate, we adopted a multi-visit observing strategy, that is, we acquired at least two spectra per night separated by at least one hour in most of the observing nights.

We reduced the data using the dedicated HARPS data reduction software and computed the cross-correlation function for each spectrum using a K5 numerical mask[57–59]. We used the data reduction software to extract the full width at half maximum (FWHM) and the bisector inverse slope (BIS) of the cross-correlation function. We measured the Ca II H and K lines activity indicator (S-index) using the code TERRA[60]. We finally extracted differential RV measurements from the HARPS spectra using the code SERVAL[61], which employs a template-matching algorithm specifically designed to derive precise radial velocities from high-resolution Echelle spectra of late K- and M-type dwarfs. The code also provides an additional activity indicator, namely, the differential line width (dLW)[61].

The HARPS SERVAL RV measurements and their uncertainties are listed in Supplementary Data 2, along with the FWHM, BIS, S-index, dLW, exposure time and S/N ratio per pixel at 550 nm. Time stamps are given in barycentric Julian date in barycentric dynamical time (BJD_{TDB}).

Frequency analysis of the HARPS RVs and activity indicators. We computed the generalized Lomb–Scargle (GLS)[62] periodogram of the HARPS RVs and used the pre-whitening technique[37,63] to subsequently identify significant peaks and remove the corresponding periodic signals from the Doppler time series. We performed a

least-squares sine fit to the amplitude and phase at the dominant frequency found by the GLS periodogram and subtracted the fit from the HARPS data. We iterated the process to identify the next most dominant frequency in the GLS periodogram of the RV residuals. We stopped the iteration once we reached the level of the noise and considered as significant only those peaks whose False Alarm Probability (FAP) is lower than 0.1%. Following the Monte Carlo bootstrap method[64], we estimated the FAP by computing the GLS periodograms of 10^6 mock datasets obtained by randomly shuffling the RV measurements, while keeping the observation time stamps fixed. We defined the FAP as the fraction of those periodograms whose highest power exceeds the power of the original observed data at any frequency.

Extended Data Figure 5 displays the GLS periodograms of the HARPS RV measurements and residuals. We found a very significant (FAP < 0.0001%, that is, no false positives out of 10^6 trials, implying a FAP < 10^{-6}) peak at frequency $f_d = 0.038\,d^{-1}$, corresponding to a period of $P_d = 26.3$ d (Extended Data Fig. 5, upper panel). The peak is surrounded by a series of equally spaced secondary peaks separated by about $0.0035\,d^{-1}$, which are aliases of the dominant frequency at $0.038\,d^{-1}$, resulting from the window function (Extended Data Fig. 5, bottom panel).

We performed a least-squares sine fit to the amplitude and phase at f_d and subtracted the best fit from the RV time series. The second panel of Extended Data Fig. 5 displays the periodogram of the residuals, following the subtraction of the signal at f_d. The most significant peak is found at frequency $f_c = 0.151\,d^{-1}$ (FAP < 0.1%), which corresponds to a period of $P_c = 6.6$ d. As in the previous case, the peak is surrounded by a series of equally spaced aliases. We iterated the pre-whitening process and found two additional significant (FAP < 0.1%) peaks at frequencies $f_e = 0.016\,d^{-1}$ ($P_e = 60.7$ d; third panel) and $f_\star = 0.023\,d^{-1}$ ($P_\star = 43.4$ d; fourth panel).

The periodograms in Extended Data Fig. 5 (right panels) show the presence of a Doppler signal at frequency $f_b = 1.824\,d^{-1}$ ($P_b = 0.55$ d)—the transiting frequency detected in the TESS light curve—whose power steadily increases once the other signals are gradually removed from the HARPS time series. This peak is associated with the Doppler reflex motion induced by the USP planet, confirming the planetary nature of the transit signal detected in TESS data. Once the 4 signals at f_c, f_d, f_e and $f_\star$ are removed from the HARPS time series (Extended Data Fig. 5, fifth panel), the peak becomes significant (FAP < 0.1%).

The periodograms of the FWHM, dLW and S-index show a significant (FAP < 0.1%) excess of power at frequencies lower than the inverse of the baseline of our measurements. An inspection of the time series unveils the presence of a long-term variation of the activity level (Extended Data Fig. 4), visible as an offset between the two observing seasons and probably associated with magnetic cycles. For each activity indicator, we accounted for the long-term variation by subtracting the seasonal median values. Extended Data Figure 6 displays the periodograms of the median-corrected activity indicators. The FWHM, dLW and S-index show significant peaks (FAP < 0.1%) between 38 and 42 days, providing strong evidence that the signal at 43.4 days seen in the HARPS RV residuals is due to stellar activity. As the same signal is also significantly detected in the Super-WASP photometry (Extended Data Fig. 7), we conclude that the stellar rotation period is 40–45 days. The signal detected in the HARPS RVs and activity indicators is associated with the presence of active regions appearing and disappearing on the visible stellar hemisphere as the star rotates about its axis.

We note that the periodograms of the activity indicators do not show any significant peaks at f_b, f_c, f_d and f_e, that is, the frequencies detected in the HARPS RVs, providing solid evidence that those signals are not associated with stellar activity, but rather they are induced by TOI-500 b and three additional, non-transiting planets with periods of ~6.6, 26.2 and 61.5 d.

Fundamental stellar parameters. We determined the stellar fundamental parameters of TOI-500 using the spectral analysis package SME (version 5.2.2; refs. [10,11]). We performed the analysis of the co-added HARPS spectrum, which has an S/N ≈ 900 in the continuum per pixel at 5,500 Å, with the MARCS model spectra[65] (https://marcs.astro.uu.se/) and the line lists from the Vienna atomic line database[66] (http://vald.astro.uu.se). The adopted methodology is the same as that described in refs. [67] and[68]. We measured the effective temperature T_{eff} from the wings of the H_α and H_β lines, and the surface gravity $\log(g_\star)$ from the Ca and Mg b triplets around 6,100 and 5,100 Å, respectively. We derived the stellar projected rotational velocity $v_\star \sin i_\star$ and the iron relative abundance [Fe/H] from the narrow unblended iron lines between 6,000 and 6,600 Å. We fixed the micro- and macro-turbulent velocities using the values provided by the calibration equations of ref. [69] ($v_{mic} = 0.5\,km\,s^{-1}$ and $v_{mac} = 1.5\,km\,s^{-1}$, respectively). We did not adopt the more recent equations from refs. [70] and [71] as they are valid only for early K, G and late F-type stars, while they are not calibrated for late K-type dwarfs such as TOI-500. We checked our best-fitting model spectrum using the Na doublet at 5,888 and 5,895 Å. We found an effective temperature of $T_{eff} = 4{,}440 \pm 100$ K, a surface gravity of $\log(g_\star) = 4.50 \pm 0.06$ cgs, an iron and calcium abundance of [Fe/H] = 0.12 ± 0.08 and [Ca/H] = −0.01 ± 0.10 and a projected rotational velocity of $v_\star \sin i_\star = 1.1 \pm 0.7\,km\,s^{-1}$.

As a sanity check, we conducted an independent spectroscopic analysis of the co-added HARPS spectrum and employed the code SpecMatch–emp[72], which utilizes hundreds of Keck/HIRES (High Resolution Echelle Spectrometer) high-resolution template spectra of FGK stars whose effective temperature, iron content and stellar radius have been accurately measured via interferometry, asteroseismology, spectral synthesis and spectrophotometry. We found an effective temperature of $T_{ef} = 4{,}400 \pm 70$ K, a stellar radius of $R_\star = 0.71 \pm 0.10\,R_\odot$ and an iron content of [Fe/H] = 0.07 ± 0.09, with the effective temperature and iron abundance in excellent agreement with the parameter estimates with SME.

We measured the interstellar extinction along the line-of-sight to TOI-500 using the method described in ref. [73]. Briefly, we built the spectral energy distribution of the star using the UBVRI[2] optical and JHKs[74] near-infrared photometry and fitted the spectral energy distribution using the BT–Settl–CIFIST[75] model spectrum with the same spectroscopic parameters as the star. We adopted the extinction law of ref. [76] and assumed a total-to-selective extinction of $R_v = A_v/E(B-V) = 3.1$ (where E(B-V) is the color excess related to the (B-V) color). We found that the interstellar reddening is negligible and consistent with zero ($A_v = 0.02 \pm 0.02$), as expected given the proximity of the star ($d \approx 47.39$ pc; ref. [1]).

We combined the effective temperature and iron abundance determined with SME with the Gaia DR2 parallax[1] and the apparent V-band magnitude[2] of $V = 10.530$ to compute the stellar mass, radius and age using the Bayesian web-tool PARAM 1.3 (ref. [12]; http://stev.oapd.inaf.it/cgi-bin/param_1.3). We added 0.06 mas to the nominal Gaia's parallax, to account for the systematic offset found by refs. [77] and [78], and we assumed an uncertainty of 0.05 on the apparent V-band magnitude. We found a stellar mass of $M_\star = 0.740 \pm 0.017\,M_\odot$ and a stellar radius of $R_\star = 0.678 \pm 0.016\,R_\odot$, implying a surface gravity of $\log(g_\star) = 4.618 \pm 0.017$ cgs in agreement within 2σ with the spectroscopic value. We also found that the stellar radius agrees with the value derived using SpecMatch–emp, corroborating our analysis. We finally used the formalism as in ref. [79] to estimate through gyrochronology the stellar age, which resulted in 5.0 ± 0.2 Gyr. This value agrees with the age of 4.7 ± 4.0 Gyr inferred with PARAM 1.3.

We also determined the local standard of rest U, V and W space velocities of the parent star using the methods of ref. [80], and, from these velocities, we computed the probability that TOI-500 belongs to the Galactic thin-disk, thick disk or halo stellar population. Using the Gaia DR2 astrometric measurements of location, parallax, proper motion and radial velocity, we derived the velocities reported in Table 1 and the following probabilities:

$$\begin{aligned} P_{thin} &= 0.92963 \pm 0.00929 \\ P_{thick} &= 0.07010 \pm 0.00002 \\ P_{halo} &= 0.0002767 \pm 0.0000008 \end{aligned} \quad (1)$$

These values are in good agreement with kinematic membership probabilities computed independently by ref. [81]. The kinematic membership of TOI-500 in the Galactic thin disk is consistent with our derived [Fe/H] and [Ca/H] values, which are typical for Galactic thin-disk stars. The main results are summarized in Table 1.

Independent transit search. To confirm the presence of the 0.55-day transiting candidate announced by the TESS team and to search for additional candidates, we independently searched the TESS light curve for transit signals. We carried out our analysis using three different detrending algorithms and methods, as described in the paragraphs below.

Method 1: we detrended the PDC-SAP light curve, filtering out stellar activity and instrumental systematics with a Savitzky–Golay filter[82], and we searched the time series for transit signals using the Détection Spécialisée de Transits algorithm[5]. While we confirmed the presence of the transiting candidate at 0.55 d, we did not identify any additional signal.

Method 2: we also searched the light curve using the detection pipeline EXOTRANS. It combines a wavelet-based filter, VARLET, to remove discontinuities and stellar variations[83] and the advanced Box-fitting Least Squares[84] (BLS), which incorporates PHALET. The latter removes previously detected transits and searches the light curve for additional periodic events. EXOTRANS can detect multiple transits or transits masked by other strong periodic events (for example, systematics or background binaries). We detected the transit signal at 0.55 d. No significant additional transit signals were detected.

Method 3: we detrended the TESS light curve with the code Wōtan[85], which implements different detrending techniques. We chose to detrend the PDC-SAP light curve by applying a cubic spline coupled to a sigma clipping algorithm, a well-known methodology for removing activity trends[86–88]. We also applied the transit least square method[6] to search for transits. Transit least square uses the transit model from Mandel and Agol[89] with the quadratic limb-darkening law. We fixed the limb-darkening coefficients of TOI-500 to the values extracted from the TESS archive. We confirmed the USP transiting-planet candidate and did not detect any additional transit signals.

The upper panel of Fig. 1 shows the median-normalized PDC-SAP light curve of TOI-500 (black points) and the spline used to detrend the TESS data (red line) following Method 3. The lower panel shows the corresponding detrended TESS light curve. The in-transit data points are highlighted with blue circles.

Joint analysis of the TESS and HARPS data. We performed the joint analysis of the TESS transit photometry and HARPS RV measurements using the code pyaneti[9], which generates posterior distributions of the fitted parameters using

Markov chain Monte Carlo simulations coupled to a Bayesian framework. Pyaneti uses the limb-darkened quadratic model from Mandel and Agol[89] for fitting the transit light curve. The code follows the q_1 and q_2 parametrization of the linear and quadratic limb-darkening coefficients u_1 and u_2 as described in ref. [90], and the parametrization of the eccentricity e and the periastron longitude ω proposed by ref. [91].

We used the PDC-SAP light curve, which was detrended following the procedure described in Method 3 in the previous section. We set Gaussian priors on q_1 and q_2 using the limb-darkening coefficients derived by ref. [92] for the TESS passband, imposing a conservative 1σ uncertainty of 0.1 on both the parameterized limb-darkening coefficients q_1 and q_2. A preliminary analysis showed that the transit light curve poorly constrains the scaled semi-major axis ($a_b/R_\star$) of planet b, owing to the shallowness of the transit signal. We therefore constrained $a_b/R_\star$ using Kepler's third law, the orbital period and a Gaussian prior on the stellar density based on the derived stellar mass and radius. For the other transit parameters, we assumed uniform priors as reported in Table 2.

The RV model follows the results presented in the frequency analysis section. Briefly, pyaneti accounts for the Doppler reflex motion of the four planets using Keplerian models. We modelled the RV stellar signal at the star's rotation period as an additional coherent, sine-like curve. We accounted for any variation not properly modelled by the coherent sine curve, and/or any instrumental noise not included in the nominal RV uncertainties, by fitting for a Doppler jitter term. We adopted uniform priors for all the RV parameters, as summarized in Table 2.

We explored the parameter space with 500 chains, 500 iterations and a chains thin factor of 10 and tested for convergence with the Gelman–Rubin statistics. If the chains do not converge, pyaneti restarts new cycles of 5,000 steps (500 iterations multiplied by the thin factor). We produced the posterior distributions from the last set of 2.5×10^5 samples once the chains reached convergence. The inferred parameter estimates are the medians of the corresponding posterior distributions, while the associated uncertainties are defined as the 68% region of the distribution credible interval. The results are reported in the fourth column of Table 2.

Figure 2 shows the phase-folded transit light curve of TOI-500 b along with the best-fitting model. The first row of Fig. 3 displays the HARPS SERVAL RV time series and the best-fitting Doppler model (stellar signal plus four planets). The second, third and fourth rows of Fig. 3 show the phase-folded HARPS SERVAL Doppler measurements and the best-fitting models for TOI-500 b, c, d, e and the star.

As a sanity check, we also estimated the Doppler reflex motion induced by the transiting planet using the floating chunk offset method described in ref. [93]. This technique is effective at measuring the mass of USP planets while filtering out the long-term RV variation induced by stellar activity and long-period objects[63,94]. Briefly, we divided the HARPS RVs into subsets of nightly measurements and analysed only those radial velocities for which multiple measurements were acquired on the same night. The best-fitting orbital solution for TOI-500 b was found using a Gaussian prior on the transit ephemeris (as derived from the modelling of the transit light curve) while allowing the RV semi-amplitude variation and nightly offsets to vary. We found a semi-amplitude of $K_b=1.38\pm0.20\,\mathrm{m\,s^{-1}}$, in very good agreement with the value reported in Table 2.

Multi-dimensional Gaussian process analysis. To study the influence of stellar activity in the HARPS RV measurements, we proceeded to analyse our dataset using a multi-dimensional Gaussian Process (GP) approach[95] as implemented in pyaneti[9,96]. This approach has been useful to distinguish planet- and activity-induced RV signals using stellar activity indicators[97].

Given the evidence of multi-signals in the RVs, we first ran a multi-dimensional GP model of the time series of the FWHM and S-index activity indicators to characterize the scales of the star-induced signal. Following ref. [95], we assumed that the FWHM and S-index time series can be modelled as

$$\begin{aligned}\Delta\mathrm{FWHM} &= F_c\,G(t),\\ \Delta\,\mathrm{S\text{-}index} &= S_c\,G(t).\end{aligned} \tag{2}$$

S_c and F_c are free parameters that relate the time series to a GP-drawn function $G(t)$ that describes the area covered by active regions on the stellar surface as a function of time. We created our co-variance matrix[95,96] using the quasi-periodic kernel

$$\gamma(t_i,t_j)=\exp\left[-\frac{\sin^2[\pi(t_i-t_j)/P_{\mathrm{GP}}]}{2\lambda_p^2}-\frac{(t_i-t_j)^2}{2\lambda_e^2}\right], \tag{3}$$

where P_{GP} is the GP characteristic period, λ_p the inverse of the harmonic complexity and λ_e is the long-term evolution timescale. We created the residual vector for the GP regression by subtracting a constant offset to each activity indicator[96].

We ran a Markov chain Monte Carlo sampling using pyaneti. We set wide Jeffreys priors on the multi-dimensional GP hyperparameters $\lambda_e\in[50,250]$ days and $\lambda_p\in[0.1,10]$, and a wide uniform prior on $P_{\mathrm{GP}}\in[30,70]$ days. Extended Data Figure 8 shows the S-index and FWHM time series along with the GP model. The inferred values for the hyperparameters are $\lambda_e=55.7^{+36.2}_{-21.2}$ days, $\lambda_p=1.5^{+1.0}_{-0.5}$ and $P_{\mathrm{GP}}=43.1^{+2.8}_{-2.6}$ days. These results suggest that the signal has low harmonic complexity and that the rotation period of the star is close to 43 days, in agreement with the periodogram analysis of the RV measurements and activity indicators and the results obtained with the Super-WASP photometry. The low harmonic complexity of the process describing the stellar signal in the activity indicators suggests that the stellar signal in the RVs has a relatively low harmonic complexity too, and a quasi-sinusoidal behaviour (see ref. [96] for more details).

We proceeded to perform an analysis including light curve and RV time series to characterize the planetary signals. For the transit modelling, we followed the same approach as the one described in the previous section. We included the RV data in the multi-dimensional GP set-up, together with the FWHM and S-index activity indicators. We assumed that the RVs, FWHM and S-index time series can be modelled as[95]

$$\begin{aligned}\Delta\mathrm{RV} &= V_c\,G(t)+V_r\,\dot{G}(t),\\ \Delta\mathrm{FWHM} &= F_c\,G(t),\\ \Delta\,\mathrm{S\text{-}index} &= S_c\,G(t),\end{aligned} \tag{4}$$

where $\dot{G}(t)$ corresponds to the time derivative of the GP-drawn function $G(t)$, while V_c and V_r are the amplitudes of $G(t)$ and $\dot{G}(t)$, respectively. The use of $\dot{G}(t)$ in the modelling is necessary to trace the active region's motion on the stellar surface[95,96]. We created the co-variance matrix in a similar way as in the previous case, using the kernel in equation (3). We also created the residual vector for the GP regression by subtracting four RV orbits accounting for the Doppler signal induced by the four planets. For the innermost planet, we set uniform priors based on the transit ephemeris (Table 2). For the other parameters of the Keplerian signals, we used wide uniform priors with period ranges based on the periodogram analysis. We note that the flexibility of this model was not able to provide a good fit for the time of inferior conjunction $T_{0,e}$ for TOI-500 e. We therefore created a weakly informative Gaussian prior based on our periodogram analysis (Table 2). For the activity indicators, we subtracted a constant offset[96]. We ran a Markov chain Monte Carlo sampling, with the same priors as before except for the GP characteristic period, where we set $P_{\mathrm{GP}}\in[35,50]$ days to speed up the convergence. Table 2 shows the priors and sampled parameters used in this analysis.

Our modelling including the RVs, FWHM and S-index recovers the Keplerian signals with periods of 0.55, 6.64, 26.23 and 61.30 days with Doppler semi-amplitudes of $K_b=1.56\pm0.20\,\mathrm{m\,s^{-1}}$, $K_c=1.95\pm0.21\,\mathrm{m\,s^{-1}}$, $K_d=8.83^{+0.25}_{-0.23}\,\mathrm{m\,s^{-1}}$ and $K_e=2.40\pm0.27\,\mathrm{m\,s^{-1}}$, respectively. These values, listed in the second column of Table 2, are consistent within 1σ with those obtained using the sinusoidal model for the stellar signal presented in the previous section. The only exceptions are the orbital period and the RV semi-amplitude induced by the outer planet (TOI-500 e), which differ by 2.2 and 1.7σ, respectively (here σ is defined as the sum in quadrature of the respective uncertainties).

As discussed before, we note that the inferred process describing the stellar RV signal has a low harmonic complexity, a relatively low amplitude $V_c=5.6^{+30.1}_{-4.1}\,\mathrm{m\,s^{-1}}$ and a low amplitude regulating the GP derivative $V_r=3^{+32}_{-19}\,\mathrm{m\,s^{-1}\,d^{-1}}$. The low-harmonic-complexity-level behaviour is in agreement with the discussion made in ref. [96]. Extended Data Figure 8 displays the time series datasets together with the inferred models. Extended Data Figure 8 shows how the activity-induced signal is well constrained by the activity indicators. Our analysis shows how, in the low harmonic regime, stellar signals behave as sinusoidal curves. Since the two analyses provide consistent results, we decided to adopt the results obtained using the simplest sinusoidal model.

Stability analysis. We carried out a set of dynamical simulations considering the gravitational interaction and the effect from general relativity to study the long-term stability of the system and check if some of the parameters, in particular those of the non-transiting planets, can be refined since they have no upper mass constraints and only lower mass limits from RVs. We took the stellar mass and radius reported in Table 1, the planetary parameters listed in Table 2 and drew hundreds of samples from the parameters posteriors as initial parameters for the dynamical simulation. We used rebound[22] with the standard IAS15 integrator[98] to integrate over 10^8 orbits for the inner planet, which correspond to a time span of ~150 kyr. The effect from general relativity was included via reboundx[23]. We could not explore a longer time span due to the highly multi-dimensional parameter space. We studied the parameter space for the non-transiting planets in more detail by drawing the true planetary masses from the reported minimum masses ($M\sin i$) listed in Table 2, allowing for inclinations between 0° and 90°, where an inclination of 90° means that the system in seen edge-on. We found that stable systems can exist for inclinations of the outer two planets TOI-500 d and e between 40° and 90°, and we could exclude orbits with inclinations $i<30°$ for planet c. Since the inner planet might have formed by inward migration via secular interaction if the outer planets form a typical Kepler multi-planet system (low eccentricities and small mutual inclinations), we studied the domain of small mutual inclinations (~4°) in more detail. In particular, we carried out dynamical simulations using the Stability of Planetary Orbital Configurations Klassifier[99] (SPOCK), which can be used to study the stability of multi-planet systems with at least 3 planets and with a maximum mutual inclination of ~11°. Since this is the case for the task at

hand, we employed SPOCK, which is much faster than rebound, allowing us to study a much longer time span. The speed-up in SPOCK is reached through the machine learning technique that is used to train stability classifications. First, numerical integration for the first 10^4 orbits is carried out and then SPOCK predicts the stability of the system over 10^9 orbits of the inner planet. We sampled the inclination of the transiting planet from the posterior solution in Table 2 and calculated, depending on the sampled inclination, the inclination for the non-transiting planets taking into account the maximal allowed mutual inclination of 11°. We took the values for the other parameters and for the USP planet from Table 1 and Table 2, and we drew 3×10^4 samples from the parameter posteriors as initial parameters for the simulation. We found that the system is stable for the whole parameter posterior space for 10^9 orbits of the inner planet, which corresponds to a time span of ~1.5 Myr.

Low-eccentricity migration process. Once all planets have formed from the protoplanetary disk and the disk is dispersed, the system undergoes a phase of secular migration, during which the eccentricities are damped and the inner planet migrates towards the star until it reaches its final orbit. The starting point for this migration would be a system of super-Earths and/or mini-Neptunes, from which the inner planet will become detached. A possible channel for the migration of USP systems accounts for an initial low eccentricity of the USP planet and its companions. To study this, we integrate the equations of motion for the secular evolution of the planets' eccentricities. We incorporate linear secular planet–planet interactions[100], which affect planets' eccentricities e_j and longitudes of pericentre ϖ_j through

$$\dot{h}_j = \frac{1}{n_j a_j^2}\frac{\partial \mathcal{R}_j}{\partial k_j}, \quad \dot{k}_j = -\frac{1}{n_j a_j^2}\frac{\partial \mathcal{R}_j}{\partial h_j}, \tag{5}$$

where $h_j = e_j \sin \varpi_j$ and $k_j = e_j \cos \varpi_j$ and h˙j and k˙j are the corresponding derivatives.TS: the dot does not go on top of the letters, Please refer above equation and fix it. Here n_j is each planet's mean motion and a_j its semi-major axis. $\mathcal{R}_j$ is the standard secular disturbing function expanded to second order in eccentricities:

$$\mathcal{R}_j = n_j a_j^2 \left[\frac{1}{2}A_{jj}\left(h_j^2 + k_j^2\right) + \sum_{k=1,k\neq j}^{4} A_{jk}\left(h_j h_k + k_j k_k\right)\right], \tag{6}$$

where the matrix elements A_{jj}, A_{jk} can be found in ref. [100]. We also incorporate general relativistic precession on all planets[30]:

$$\dot{\varpi}_j = \frac{3GM_\star n_j}{c^2 a_j}, \tag{7}$$

c being the speed of light and G the gravitational constant. On the innermost planet we also include terms for tidal precession[30]:

$$\dot{\varpi}_\mathrm{b} = \frac{15 k_{2,\mathrm{b}} n_\mathrm{b}}{2}\frac{M_\star}{m_\mathrm{b}}\left(\frac{R_\mathrm{b}}{a_\mathrm{b}}\right)^5, \tag{8}$$

where $k_{2,\mathrm{b}} = 1$ is the tidal Love number, and for decay of eccentricity and semi-major axis through tidal forces raised on the planet[101]:

$$\dot{e}_\mathrm{b} = -\frac{63\sqrt{GM_\star^3}R_\mathrm{b}^5}{4Q_\mathrm{b} m_\mathrm{b} a_\mathrm{b}^{13/2}} e_\mathrm{b}, \quad \dot{a}_\mathrm{b} = -\frac{63\sqrt{GM_\star^3}R_\mathrm{b}^5}{2Q_\mathrm{b} m_\mathrm{b} a_\mathrm{b}^{13/2}} e_\mathrm{b}^2 a_\mathrm{b}, \tag{9}$$

respectively, where $Q_\mathrm{b} = 100$ is the (constant) tidal quality factor (for comparison, for Earth $Q/k \approx 1{,}000$ (ref. [102]), for the Moon $Q/k \approx 1{,}600$ (ref. [103]), for Mars $Q/k \approx 600$ (ref. [104]) and for Io $Q/k \approx 70$ (ref. [105]). These equations are converted to (h_j, k_j) coordinates and integrated with the scipy Dormand–Price integrator[106].

We explored a range of initial semi-major axes for TOI-500 b from 0.02 to 0.03 au and initial eccentricities $e_\mathrm{b} = 0.05$, $e_\mathrm{c} = 0.05$, $e_\mathrm{d} \in \{0.05, 0.1\}$ and $e_\mathrm{c} \in \{0.05, 0.1, 0.15, 0.2, 0.25\}$. Initial longitudes of pericentre for the planets were set to 0, 90, 180 and 270 deg. The equations were integrated for a time of 5 Gyr, or until the semi-major axis of TOI-500 b attained its current value.

We found that migration to the present location is possible within 5 Gyr so long as the initial eccentricities of the planets are sufficiently high ($e_\mathrm{c} \gtrsim 0.2$ when $e_\mathrm{b} = e_\mathrm{c} = e_\mathrm{d} = 0.05$). When the initial $a_\mathrm{b} \gtrsim 0.25$ au, the eccentricities of the two innermost planets can be excited high enough for their orbits to overlap. This renders the secular approximation described here invalid, although migration of TOI-500 b to its current orbit may still be possible if collisions between the planets do not occur. With $a_\mathrm{b} \lesssim 0.25$ au, orbit-crossing is avoided. We show one example of migration in Fig. 6, starting at $a_\mathrm{b} = 0.02$ au. Initial migration is rapid, with the planet migrating from 0.02 to 0.013 au in around 100 Myr, after which it slows. The present semi-major axis is attained after 2 Gyr, at which time migration is still proceeding, albeit very slowly. We also show in Fig. 6 an analytical, high-eccentricity migration track, where the planet is placed on a high-eccentricity orbit and circularizes while maintaining its orbital angular momentum, emphasizing the qualitatively different nature of the low-eccentricity pathway.

Atmospheric characterization of TOI-500 b. Ultra-short-period planets present the intriguing possibility of atmospheric characterization to study secondary atmosphere creation[107], extreme star–planet interactions[108] and to get clues as to the dynamical and migration history of the planet[31]. In addition, given their extremely short period and frequent transits, they are attractive for atmospheric characterization from an observational perspective. Ultra-short-period planets might have three different types of atmosphere: a Mercury-type atmosphere[109], a lava-ocean atmosphere[110–112] or a silicate atmosphere[113–115]. It would be very interesting to detect the atmosphere of TOI-500 b because in all three cases the atmosphere would contain material from the crust or even the interior of the planet. The detection of its atmosphere would thus open up the thrilling possibility to do mineralogy of an extrasolar planet. TOI-500 b is among the top 10 targets (currently ranked 8th) for hot terrestrial super-Earth planets (that is, planets with radius $R_\mathrm{p} < 2\,R_\oplus$ and equilibrium temperature $T_\mathrm{eq} > 1{,}000$ K), joining targets GJ 367 b, 55 Cnc e, HD 219134 b, K2-141 b, GJ 1252 b, TOI-1807 b, TOI-561 b, TOI-1685 b and GJ 9827 b. Extended Data Figure 9 displays a relative atmospheric detection S/N metric (normalized to TOI-500 b) for all well-characterized transiting planets with $R_\mathrm{p} < 2\,R_\oplus$. The sample of exoplanets is taken from the NASA Exoplanet Archive (available at https://exoplanetarchive.ipac.caltech.edu/). The atmospheric signal is calculated in a similar way in ref. [116] and is dominated by the atmospheric scale height, favoring hot, extended atmospheres, and the host-star radius, favoring small, cool stars. The relative S/N calculation scales with properties that make it favourable to detect and measure this signal. Our metric is similar to the transmission spectroscopy metric in ref. [117]. The difference with our metric is that instead of calculating this per transit we calculate it based on time, thus adding a $P^{-0.5}$ term. Given the observational challenges of observing planets in transit with highly oversubscribed facilities, the frequency of transits is a very important constraint on obtaining atmospheric measurements of these exoplanets. We assume an effective scale height ($h_\mathrm{eff} = 7H$, with H the Earth scale height, ref. [118]) using the equilibrium temperature, a Bond albedo of $\alpha = 0.3$ and an atmospheric mean molecular weight of $\mu = 20$. Because this is a relative assessment, and we are assuming identical properties for all the atmospheres in this sample, the precise values of these variables do not change the results. Silicate atmospheres of hot lava-ocean worlds should be detectable in lines of Na, O_2, O and SiO (ref. [113]). Clearly, there are likely to be interesting variations in atmospheric properties among these exoplanets, which is precisely why it is important to observe a population of hot lava-ocean worlds like TOI-500 b.

Data availability

TESS photometry is available at the Mikulski Archive for Space Telescopes (MAST) at https://exo.mast.stsci.edu under target name TOI-500.01. The raw HARPS spectra can be retrieved from the ESO Science Archive Facility (http://archive.eso.org/cms.html) under ESO programme IDs 1102.C-0923 (PI: D.G.), 0103.C-0442 (PI: M.R.D.), 0102.C-0338 and 0103.C-0548 (PI: T.T.), and 60.A-9700 and 60.A-9709 (ESO technical time). The ground-based photometry obtained with the LCO telescope, as well as the SOAR and Gemini imaging data, are available on the Exoplanet Follow-up Observing Program (ExoFOP) website (https://exofop.ipac.caltech.edu/tess/) under target name TOI-500.01. The raw Gemini data are available at https://archive.gemini.edu/searchform under Program ID GS-2020A-Q-125. The archival WASP data that support the findings of this study are available from the co-author C. Hellier upon reasonable request (c.hellier@keele.ac.uk). The archival SOAR data that support the findings of this study are available from the co-author C. Ziegler (carlziegler@gmail.com) upon reasonable request. The extracted radial velocities and stellar activity indicators are listed in Supplementary Data 2.

Code availability

The numerical code used to test the low-eccentricity migration pathway is available via Zenodo at https://doi.org/10.5281/zenodo.5877066.

Received: 6 August 2021; Accepted: 23 February 2022;
Published online: 28 April 2022

References

1. Gaia Collaboration et al. Gaia data release 2. Summary of the contents and survey properties. *Astron. Astrophys.* **616**, A1 (2018).
2. Mermilliod, J. C. UBV photoelectric photometry catalogue (1986): I. The original data. *Astron. Astrophys. Suppl. Ser.* **71**, 413 (1987).
3. Ricker, G. R. et al. Transiting Exoplanet Survey Satellite (TESS). *J. Astro. Telesc. Instrum. Syst.* **1**, 014003 (2015).
4. Jenkins, J. M. et al. The TESS science processing operations center. *Proc. SPIE Int. Soc. Opt. Eng.* **9913**, 93133E (2016).
5. Cabrera, J., Csizmadia, S., Erikson, A., Rauer, H. & Kirste, S. A study of the performance of the transit detection tool DST in space-based surveys. Application of the CoRoT pipeline to Kepler data. *Astron. Astrophys.* **548**, A44 (2012).
6. Hippke, M. & Heller, R. Optimized transit detection algorithm to search for periodic transits of small planets. *Astron. Astrophys.* **623**, A39 (2019).

7. Brown, T. M. et al. Las Cumbres Observatory Global Telescope Network. *Publ. Astron. Soc. Pac.* **125**, 1031 (2013).
8. Mayor, M. et al. Setting new standards with HARPS. *The Messenger* **114**, 20–24 (2003).
9. Barragán, O., Gandolfi, D. & Antoniciello, G. PYANETI: a fast and powerful software suite for multiplanet radial velocity and transit fitting. *Mon. Not. R. Astron. Soc.* **482**, 1017–1030 (2019).
10. Valenti, J. A. & Piskunov, N. Spectroscopy made easy: a new tool for fitting observations with synthetic spectra. *Astron. Astrophys. Suppl. Ser.* **118**, 595–603 (1996).
11. Piskunov, N. & Valenti, J. A. Spectroscopy made easy: evolution. *Astron. Astrophys.* **597**, A16 (2017).
12. da Silva, L. et al. Basic physical parameters of a selected sample of evolved stars. *Astron. Astrophys.* **458**, 609–623 (2006).
13. Pollacco, D. L. et al. The WASP project and the SuperWASP cameras. *Publ. Astron. Soc. Pac.* **118**, 1407–1418 (2006).
14. Oelkers, R. J. et al. Variability properties of four million sources in the TESS input catalog observed with the Kilodegree Extremely Little Telescope survey. *Astron. J.* **155**, 39 (2018).
15. Pepe, F. et al. An Earth-sized planet with an Earth-like density. *Nature* **503**, 377–380 (2013).
16. Léger, A. et al. Transiting exoplanets from the CoRoT space mission. VIII. CoRoT-7b: the first super-Earth with measured radius. *Astron. Astrophys.* **506**, 287–302 (2009).
17. Winn, J. N., Sanchis-Ojeda, R. & Rappaport, S. Kepler-78 and the ultra-short-period planets. *New Astron. Rev.* **83**, 37–48 (2018).
18. Lam, K. W. F. et al. GJ 367b: a dense, ultrashort-period sub-Earth planet transiting a nearby red dwarf star. *Science* **374**, 1271–1275 (2021).
19. Tabernero, H. M. et al. HORuS transmission spectroscopy of 55 Cnc e. *Mon. Not. R. Astron. Soc.* **498**, 4222–4229 (2020).
20. Madhusudhan, N. & Redfield, S. Optimal measures for characterizing water-rich super-Earths. *Int. J. Astrobiol.* **14**, 177–189 (2015).
21. Otegi, J. F., Bouchy, F. & Helled, R. Revisited mass–radius relations for exoplanets below 120 $M_{\oplus}$. *Astron. Astrophys.* **634**, A43 (2020).
22. Rein, H. & Liu, S. F. REBOUND: an open-source multi-purpose N-body code for collisional dynamics. *Astron. Astrophys.* **537**, A128 (2012).
23. Tamayo, D., Rein, H., Shi, P. & Hernandez, D. M. REBOUNDx: a library for adding conservative and dissipative forces to otherwise symplectic N-body integrations. *Mon. Not. R. Astron. Soc.* **491**, 2885–2901 (2020).
24. Isella, A., Testi, L. & Natta, A. Large dust grains in the inner region of circumstellar disks. *Astron. Astrophys.* **451**, 951–959 (2006).
25. Schlaufman, K. C. Evidence of possible spin-orbit misalignment along the line of sight in transiting exoplanet systems. *Astrophys. J.* **719**, 602–611 (2010).
26. Steffen, J. H. & Farr, W. M. A lack of short-period multiplanet systems with close-proximity pairs and the curious case of Kepler-42. *Astrophys. J.* **774**, L12 (2013).
27. Dai, F., Masuda, K. & Winn, J. N. Larger mutual inclinations for the shortest-period planets. *Astrophys. J.* **864**, L38 (2018).
28. Lee, E. J. & Chiang, E. Magnetospheric truncation, tidal inspiral, and the creation of short-period and ultra-short-period planets. *Astrophys. J.* **842**, 40 (2017).
29. Petrovich, C., Deibert, E. & Wu, Y. Ultra-short-period planets from secular chaos. *Astron. J.* **157**, 180 (2019).
30. Pu, B. & Lai, D. Low-eccentricity migration of ultra-short-period planets in multiplanet systems. *Mon. Not. R. Astron. Soc.* **488**, 3568–3587 (2019).
31. Millholland, S. C. & Spalding, C. Formation of ultra-short-period planets by obliquity-driven tidal runaway. *Astrophys. J.* **905**, 71 (2020).
32. Laskar, J. Large scale chaos and the spacing of the inner planets. *Astron. Astrophys.* **317**, L75–L78 (1997).
33. Fabrycky, D. C. et al. Transit timing observations from Kepler. IV. Confirmation of four multiple-planet systems by simple physical models. *Astrophys. J.* **750**, 114 (2012).
34. Kamiaka, S. et al. The misaligned orbit of the Earth-sized planet Kepler-408b. *Astron. J.* **157**, 137 (2019).
35. Lacedelli, G. et al. An unusually low density ultra-short period super-Earth and three mini-Neptunes around the old star TOI-561. *Mon. Not. R. Astron. Soc.* **501**, 4148–4166 (2021).
36. Queloz, D. et al. The CoRoT-7 planetary system: two orbiting super-Earths. *Astron. Astrophys.* **506**, 303–319 (2009).
37. Hatzes, A. P. et al. An investigation into the radial velocity variations of CoRoT-7. *Astron. Astrophys.* **520**, A93 (2010).
38. Haywood, R. D. et al. Planets and stellar activity: hide and seek in the CoRoT-7 system. *Mon. Not. R. Astron. Soc.* **443**, 2517–2531 (2014).
39. Faria, J. P. et al. Uncovering the planets and stellar activity of CoRoT-7 using only radial velocities. *Astron. Astrophys.* **588**, A31 (2016).
40. Smith, J. C. et al. Kepler presearch data conditioning II—a Bayesian approach to systematic error correction. *Publ. Astron. Soc. Pac.* **124**, 1000 (2012).
41. Stumpe, M. C. et al. Kepler presearch data conditioning I. Architecture and algorithms for error correction in Kepler light curves. *Publ. Astron. Soc. Pac.* **124**, 985 (2012).
42. Stumpe, M. C. et al. Multiscale systematic error correction via wavelet-based bandsplitting in Kepler Data. *Publ. Astron. Soc. Pac.* **126**, 100 (2014).
43. Twicken, J. D. et al. Kepler data validation I. Architecture, diagnostic tests, and data products for vetting transiting planet candidates. *Publ. Astron. Soc. Pac.* **130**, 064502 (2018).
44. Li, J. et al. Kepler data validation II—transit model fitting and multiple-planet search. *Publ. Astron. Soc. Pac.* **131**, 024506 (2019).
45. McCully, C. et al. Real-time processing of the imaging data from the network of Las Cumbres Observatory Telescopes using BANZAI. (eds. Guzman, J. C. and Ibsen, J.) Software and Cyberinfrastructure for Astronomy V, *Proc SPIE* Vol. 10707 107070K (2018).
46. Collins, K. A., Kielkopf, J. F., Stassun, K. G. & Hessman, F. V. AstroImageJ: image processing and photometric extraction for ultra-precise astronomical light curves. *Astron. J.* **153**, 77 (2017).
47. Maxted, P. F. L. et al. WASP-41b: a transiting hot Jupiter planet orbiting a magnetically active G8V star. *Publ. Astron. Soc. Pac.* **123**, 547 (2011).
48. Ciardi, D. R., Beichman, C. A., Horch, E. P. & Howell, S. B. Understanding the effects of stellar multiplicity on the derived planet radii from transit surveys: implications for Kepler, K2, and TESS. *Astrophys. J.* **805**, 16 (2015).
49. Scott, N. J. 'Alopeke, Zorro, and NESSI: three dual-channel speckle imaging instruments at Gemini-North, Gemini-South, and the WIYN telescopes. In *AAS/Division for Extreme Solar Systems Abstracts*, Bulletin of the American Astronomical Society, Vol. 51 330.15 (2019).
50. Howell, S. B., Everett, M. E., Sherry, W., Horch, E. & Ciardi, D. R. Speckle camera observations for the NASA Kepler mission follow-up program. *Astron. J.* **142**, 19 (2011).
51. Tokovinin, A. Ten years of speckle interferometry at SOAR. *Publ. Astron. Soc. Pac.* **130**, 035002 (2018).
52. Ziegler, C. et al. SOAR TESS survey. I. Sculpting of TESS planetary systems by stellar companions. *Astron. J.* **159**, 19 (2020).
53. Martin, R. G. et al. The Kozai–Lidov mechanism in hydrodynamical disks. *Astrophys. J.* **792**, L33 (2014).
54. Jang-Condell, H. On the likelihood of planet formation in close binaries. *Astrophys. J.* **799**, 147 (2015).
55. Cieza, L. A. et al. Primordial circumstellar disks in binary systems: evidence for reduced lifetimes. *Astrophys. J.* **696**, L84–L88 (2009).
56. Kraus, A. L., Ireland, M. J., Hillenbrand, L. A. & Martinache, F. The role of multiplicity in disk evolution and planet formation. *Astrophys. J.* **745**, 19 (2012).
57. Baranne, A. et al. ELODIE: a spectrograph for accurate radial velocity measurements. *Astron. Astrophys. Suppl. Ser.* **119**, 373–390 (1996).
58. Pepe, F. et al. The CORALIE survey for southern extra-solar planets VII. Two short-period Saturnian companions to HD 108147 and HD 168746. *Astron. Astrophys.* **388**, 632–638 (2002).
59. Lovis, C. & Pepe, F. A new list of thorium and argon spectral lines in the visible. *Astron. Astrophys.* **468**, 1115–1121 (2007).
60. Anglada-Escudé, G. & Butler, R. P. The HARPS-TERRA project. I. Description of the algorithms, performance, and new measurements on a few remarkable stars observed by HARPS. *Astrophys. J. Suppl. Ser.* **200**, 15 (2012).
61. Zechmeister, M. et al. Spectrum radial velocity analyser (SERVAL). High-precision radial velocities and two alternative spectral indicators. *Astron. Astrophys.* **609**, A12 (2018).
62. Zechmeister, M. & Kürster, M. The generalised Lomb–Scargle periodogram. A new formalism for the floating-mean and Keplerian periodograms. *Astron. Astrophys.* **496**, 577–584 (2009).
63. Gandolfi, D. et al. The transiting multi-planet system HD 3167: A 5.7 $M_{\oplus}$ super-Earth and an 8.3 $M_{\oplus}$ mini-Neptune. *Astron. J.* **154**, 123 (2017).
64. Murdoch, K. A., Hearnshaw, J. B. & Clark, M. A search for substellar companions to southern solar-type stars. *Astrophys. J.* **413**, 349 (1993).
65. Gustafsson, B. et al. A grid of MARCS model atmospheres for late-type stars. I. Methods and general properties. *Astron. Astrophys.* **486**, 951–970 (2008).
66. Ryabchikova, T. et al. A major upgrade of the VALD database. *Phys. Scr.* **90**, 054005 (2015).
67. Fridlund, M. et al. K2-111 b—a short period super-Earth transiting a metal poor, evolved old star. *Astron. Astrophys.* **604**, A16 (2017).
68. Persson, C. M. et al. Super-Earth of 8 $M_{\oplus}$ in a 2.2-day orbit around the K5V star K2-216. *Astron. Astrophys.* **618**, A33 (2018).
69. Gray, D. F. Measurements of rotation and turbulence in F, G and K dwarfs. *Astrophys. J.* **281**, 719–722 (1984).
70. Bruntt, H. et al. Accurate fundamental parameters for 23 bright solar-type stars. *Mon. Not. R. Astron. Soc.* **405**, 1907–1923 (2010).
71. Doyle, A. P., Davies, G. R., Smalley, B., Chaplin, W. J. & Elsworth, Y. Determining stellar macroturbulence using asteroseismic rotational velocities from Kepler. *Mon. Not. R. Astron. Soc.* **444**, 3592–3602 (2014).

72. Yee, S. W., Petigura, E. A. & von Braun, K. Precision stellar characterization of FGKM stars using an empirical spectral library. *Astrophys. J.* **836**, 77 (2017).
73. Gandolfi, D. et al. The star formation in the L1615/L1616 cometary cloud. *Astrophys. J.* **687**, 1303–1322 (2008).
74. Cutri, R. M. et al. *2MASS All Sky Catalog of Point Sources. VizieR Online Data Catalog* (2003).
75. Baraffe, I., Homeier, D., Allard, F. & Chabrier, G. New evolutionary models for pre-main sequence and main sequence low-mass stars down to the hydrogen-burning limit. *Astron. Astrophys.* **577**, A42 (2015).
76. Cardelli, J. A., Clayton, G. C. & Mathis, J. S. The relationship between infrared, optical, and ultraviolet extinction. *Astrophys. J.* **345**, 245 (1989).
77. Stassun, K. G. & Torres, G. Evidence for a systematic offset of −80 μas in the Gaia DR2 parallaxes. *Astrophys. J.* **862**, 61 (2018).
78. Zinn, J. C., Pinsonneault, M. H., Huber, D. & Stello, D. Confirmation of the Gaia DR2 parallax zero-point offset using asteroseismology and spectroscopy in the Kepler field. *Astrophys. J.* **878**, 136 (2019).
79. Mamajek, E. E. & Hillenbrand, L. A. Improved age estimation for solar-type dwarfs using activity-rotation diagnostics. *Astrophys. J.* **687**, 1264–1293 (2008).
80. Reddy, B. E., Lambert, D. L. & Allende Prieto, C. Elemental abundance survey of the Galactic thick disc. *Mon. Not. R. Astron. Soc.* **367**, 1329–1366 (2006).
81. Carrillo, A., Hawkins, K., Bowler, B. P., Cochran, W. & Vanderburg, A. Know thy star, know thy planet: chemo-kinematically characterizing TESS targets. *Mon. Not. R. Astron. Soc.* **491**, 4365–4381 (2020).
82. Savitzky, A. & Golay, M. J. E. Smoothing and differentiation of data by simplified least squares procedures. *Anal. Chem.* **36**, 1627–1639 (1964).
83. Grziwa, S. et al. K2-31B, a grazing transiting hot Jupiter on a 1.26-day orbit around a bright G7V star. *Astron. J.* **152**, 132 (2016).
84. Kovács, G., Zucker, S. & Mazeh, T. BLS: Box-fitting Least Squares (ASCL, 2016).
85. Hippke, M., David, T. J., Mulders, G. D. & Heller, R. Wōtan: comprehensive time-series detrending in Python. *Astron. J.* **158**, 143 (2019).
86. Burt, J. A. et al. TOI-824 b: a new planet on the lower edge of the hot Neptune desert. *Astron. J.* **160**, 153 (2020).
87. Wong, I. et al. Systematic phase curve study of known transiting systems from year one of the TESS mission. *Astron. J.* **160**, 155 (2020).
88. Ikwut-Ukwa, M. et al. The K2 and TESS synergy. I. Updated ephemerides and parameters for K2-114, K2-167, K2-237, and K2-261. *Astron. J.* **160**, 209 (2020).
89. Mandel, K. & Agol, E. Analytic light curves for planetary transit searches. *Astrophys. J.* **580**, L171–L175 (2002).
90. Kipping, D. M. Efficient, uninformative sampling of limb darkening coefficients for two-parameter laws. *Mon. Not. R. Astron. Soc.* **435**, 2152–2160 (2013).
91. Anderson, D. R. et al. Thermal emission at 4.5 and 8 μm of WASP-17b, an extremely large planet in a slightly eccentric orbit. *Mon. Not. R. Astron. Soc.* **416**, 2108–2122 (2011).
92. Claret, A. Limb and gravity-darkening coefficients for the TESS satellite at several metallicities, surface gravities, and microturbulent velocities. *Astron. Astrophys.* **600**, A30 (2017).
93. Hatzes, A. P. et al. The mass of CoRoT-7b. *Astrophys. J.* **743**, 75 (2011).
94. Barragán, O. et al. K2-141 b. A 5-$M_{\oplus}$ super-Earth transiting a K7 V star every 6.7 h. *Astron. Astrophys.* **612**, A95 (2018).
95. Rajpaul, V., Aigrain, S., Osborne, M. A., Reece, S. & Roberts, S. A Gaussian process framework for modelling stellar activity signals in radial velocity data. *Mon. Not. R. Astron. Soc.* **452**, 2269–2291 (2015).
96. Barragán, O., Aigrain, S., Rajpaul, V. M. & Zicher, N. pyaneti II: A multi-dimensional Gaussian process approach to analysing spectroscopic time-series. *Mon. Not. R. Astron. Soc.* **9**, 866–883 (2021).
97. Barragán, O. et al. Radial velocity confirmation of K2-100b: a young, highly irradiated, and low-density transiting hot Neptune. *Mon. Not. R. Astron. Soc.* **490**, 698–708 (2019).
98. Rein, H. & Spiegel, D. S. IAS15: a fast, adaptive, high-order integrator for gravitational dynamics, accurate to machine precision over a billion orbits. *Mon. Not. R. Astron. Soc.* **446**, 1424–1437 (2015).
99. Tamayo, D. et al. Predicting the long-term stability of compact multiplanet systems. *Proc. Natl Acad. Sci. USA* **117**, 18194–18205 (2020).
100. Murray, C. D. & Dermott, S. F. *Solar System Dynamics*, Cambridge University Press (1999).
101. Jackson, B., Greenberg, R. & Barnes, R. Tidal evolution of close-in extrasolar planets. *Astrophys. J.* **678**, 1396–1406 (2008).
102. Ray, R. D., Eanes, R. J. & Lemoine, F. G. Constraints on energy dissipation in the Earth's body tide from satellite tracking and altimetry. *Geophys. J. Int.* **144**, 471–480 (2001).
103. Williams, J. G. et al. Lunar interior properties from the GRAIL mission. *J. Geophys. Res. Planets* **119**, 1546–1578 (2014).
104. Jacobson, R. A. & Lainey, V. Martian satellite orbits and ephemerides. *Planet. Space Sci.* **102**, 35–44 (2014).
105. Lainey, V., Arlot, J.-E., Karatekin, Ö. & van Hoolst, T. Strong tidal dissipation in Io and Jupiter from astrometric observations. *Nature* **459**, 957–959 (2009).
106. Virtanen, P. et al. SciPy 1.0: fundamental algorithms for scientific computing in Python. *Nat. Methods* **17**, 261–272 (2020).
107. Owen, J. E. & Wu, Y. Atmospheres of low-mass planets: the "boil-off". *Astrophys. J.* **817**, 107 (2016).
108. Cauley, P. W., Redfield, S. & Jensen, A. G. A decade of Hα transits for HD 189733 b: stellar activity versus absorption in the extended atmosphere. *Astron. J.* **153**, 217 (2017).
109. Mura, A. et al. Comet-like tail-formation of exospheres of hot rocky exoplanets: possible implications for CoRoT-7b. *Icarus* **211**, 1–9 (2011).
110. Briot, D. & Schneider, J. Occurrence, physical conditions, and observations of super-Ios and hyper-Ios. In *Astronomical Society of the Pacific Conference Series* Vol. 430 (eds. Foresto, V. C. du et al.) The Society, 409 (2010).
111. Rouan, D. et al. The orbital phases and secondary transits of Kepler-10b. A physical interpretation based on the lava-ocean planet model. *Astrophys. J.* **741**, L30 (2011).
112. Barnes, R., Raymond, S. N., Greenberg, R., Jackson, B. & Kaib, N. A. CoRoT-7b: super-Earth or super-Io? *Astrophys. J.* **709**, L95–L98 (2010).
113. Schaefer, L. & Fegley, B. Chemistry of silicate atmospheres of evaporating super-Earths. *Astrophys. J.* **703**, L113–L117 (2009).
114. Ito, Y. et al. Theoretical emission spectra of atmospheres of hot rocky super-Earths. *Astrophys. J.* **801**, 144 (2015).
115. Miguel, Y. Observability of molecular species in a nitrogen dominated atmosphere for 55 Cancri e. *Mon. Not. R. Astron. Soc.* **482**, 2893–2901 (2019).
116. Niraula, P. et al. Three super-Earths transiting the nearby star GJ 9827. *Astron. J.* **154**, 266 (2017).
117. Kempton, E. M. R. et al. A framework for prioritizing the TESS planetary candidates most amenable to atmospheric characterization. *Publ. Astron. Soc. Pac.* **130**, 114401 (2018).
118. Miller-Ricci, E., Meyer, M. R., Seager, S. & Elkins-Tanton, L. On the emergent spectra of hot protoplanet collision afterglows. *Astrophys. J.* **704**, 770–780 (2009).
119. Cutri, R. M. et al. *VizieR Online Data Catalog: AllWISE Data Release (Cutri+ 2013)* (February 2021).
120. Southworth, J. et al. Kepler photometry of KIC 10661783: a binary star with total eclipses and δ Scuti pulsations. *Mon. Not. R. Astron. Soc.* **414**, 2413–2423 (2011).
121. Zeng, L., Sasselov, D. D. & Jacobsen, S. B. Mass–radius relation for rocky planets based on PREM. *Astrophys. J.* **819**, 127 (2016).
122. Southworth, J. Homogeneous studies of transiting extrasolar planets—IV. Thirty systems with space-based light curves. *Mon. Not. R. Astron. Soc.* **417**, 2166–2196 (2011).
123. Malavolta, L. et al. An ultra-short period rocky super-Earth with a secondary eclipse and a Neptune-like companion around K2-141. *Astron. J.* **155**, 107 .(2018).
124. Mann, A. W. et al. The gold standard: accurate stellar and planetary parameters for eight Kepler M dwarf systems enabled by parallaxes. *Astron. J.* **153**, 267 (2017).
125. Muirhead, P. S. et al. Characterizing the cool KOIs. III. KOI 961: a small star with large proper motion and three small planets. *Astrophys. J.* **747**, 144 (2012).
126. Livingston, J. H. et al. Sixty validated planets from K2 campaigns 5–8. *Astron. J.* **156**, 277 (2018).
127. Adams, E. R. et al. Ultra-short-period planets in K2 with companions: a double transiting system for EPIC 220674823. *Astron. J.* **153**, 82 (2017).
128. Sinukoff, E. et al. K2-66b and K2-106b: two extremely hot sub-Neptune-size planets with high densities. *Astron. J.* **153**, 271 (2017).
129. Guenther, E. W. et al. K2-106, a system containing a metal-rich planet and a planet of lower density. *Astron. Astrophys.* **608**, A93 (2017).
130. Santerne, A. et al. An Earth-sized exoplanet with a Mercury-like composition. *Nat. Astron.* **2**, 393–400 (2018).
131. Marcy, G. W. et al. Masses, radii, and orbits of small Kepler planets: the transition from gaseous to rocky planets. *Astrophys. J. Suppl. Ser.* **210**, 20 (2014).
132. Butler, R. P., Marcy, G. W., Williams, E., Hauser, H. & Shirts, P. Three new "51 Pegasi-type" planets. *Astrophys. J.* **474**, L115–L118 (1997).
133. McArthur, B. E. et al. Detection of a Neptune-mass planet in the ρ^1 Cancri system using the Hobby–Eberly telescope. *Astrophys. J.* **614**, L81–L84 (2004).
134. Marcy, G. W. et al. A planet at 5 AU around 55 Cancri. *Astrophys. J.* **581**, 1375–1388 (2002).
135. Fischer, D. A. et al. Five planets orbiting 55 Cancri. *Astrophys. J.* **675**, 790–801 (2008).
136. von Braun, K. et al. 55 Cancri: stellar astrophysical parameters, a planet in the habitable zone, and implications for the radius of a transiting super-Earth. *Astrophys. J.* **740**, 49 (2011).
137. Winn, J. N. et al. A super-Earth transiting a naked-eye star. *Astrophys. J.* **737**, L18 (2011).

138. Nowak, G. et al. The CARMENES search for exoplanets around M dwarfs. Two planets on opposite sides of the radius gap transiting the nearby M dwarf LTT 3780. *Astron. Astrophys.* **642**, A173 (2020).
139. Cloutier, R. et al. A pair of TESS planets spanning the radius valley around the nearby mid-M dwarf LTT 3780. *Astron. J.* **160**, 3 (2020).
140. Hellier, C. et al. Seven transiting hot Jupiters from WASP-South, Euler and TRAPPIST: WASP-47b, WASP-55b, WASP-61b, WASP-62b, WASP-63b, WASP-66b and WASP-67b. *Mon. Not. R. Astron. Soc.* **426**, 739–750 (2012).
141. Sanchis-Ojeda, R. et al. A low stellar obliquity for WASP-47, a compact multiplanet system with a hot Jupiter and an ultra-short period planet. *Astrophys. J.* **812**, L11 (2015).
142. Becker, J. C., Vanderburg, A., Adams, F. C., Rappaport, S. A. & Schwengeler, H. M. WASP-47: a hot Jupiter system with two additional planets discovered by K2. *Astrophys. J.* **812**, L18 (2015).
143. Almenara, J. M., Díaz, R. F., Bonfils, X. & Udry, S. Absolute densities, masses, and radii of the WASP-47 system determined dynamically. *Astron. Astrophys.* **595**, L5 (2016).
144. Neveu-VanMalle, M. et al. Hot Jupiters with relatives: discovery of additional planets in orbit around WASP-41 and WASP-47. *Astron. Astrophys.* **586**, A93 (2016).
145. Vanderburg, A. et al. Precise masses in the WASP-47 system. *Astron. J.* **154**, 237 (2017).
146. Batalha, N. M. et al. Kepler's first rocky planet: Kepler-10b. *Astrophys. J.* **729**, 27 (2011).
147. Fressin, F. et al. Kepler-10 c: a 2.2 Earth radius transiting planet in a multiple system. *Astrophys. J. Suppl. Ser.* **197**, 5 (2011).
148. Santos, N. C. et al. Constraining planet structure from stellar chemistry: the cases of CoRoT-7, Kepler-10, and Kepler-93. *Astron. Astrophys.* **580**, L13 (2015).
149. Fogtmann-Schulz, A. et al. Accurate parameters of the oldest known rocky-exoplanet hosting system: Kepler-10 revisited. *Astrophys. J.* **781**, 67 (2014).
150. Weiss, L. M. et al. Revised masses and densities of the planets around Kepler-10. *Astrophys. J.* **819**, 83 (2016).
151. Rajpaul, V., Buchhave, L. A. & Aigrain, S. Pinning down the mass of Kepler-10c: the importance of sampling and model comparison. *Mon. Not. R. Astron. Soc.* **471**, L125–L130 (2017).
152. Barros, S. C. C. et al. Revisiting the transits of CoRoT-7b at a lower activity level. *Astron. Astrophys.* **569**, A74 (2014).
153. Vanderburg, A. et al. Two small planets transiting HD 3167. *Astrophys. J.* **829**, L9 (2016).
154. Christiansen, J. L. et al. Three's company: an additional non-transiting super-Earth in the bright HD 3167 system, and masses for all three planets. *Astron. J.* **154**, 122 (2017).
155. Stassun, K. G. et al. The TESS input catalog and candidate target list. *Astron. J.* **156**, 102 (2018).
156. Espinoza, N. et al. HD 213885b: a transiting 1-d-period super-Earth with an Earth-like composition around a bright (V = 7.9) star unveiled by TESS. *Mon. Not. R. Astron. Soc.* **491**, 2982–2999 (2020).

Acknowledgements

This work was supported by the KESPRINT (www.kesprint.science) collaboration, an international consortium devoted to the characterization and research of exoplanets discovered with space-based missions. This paper includes data collected by the TESS mission. Funding for the TESS mission is provided by the NASA Explorer Program. We acknowledge the use of TESS Alert data, which is currently in a beta test phase, from pipelines at the TESS Science Office and at the TESS Science Processing Operations Center. Resources supporting this work were provided by the NASA High-End Computing Program through the NASA Advanced Supercomputing Division at Ames Research Center for the production of the SPOC data products. This research has made use of the Exoplanet Follow-up Observation Program website, which is operated by the California Institute of Technology, under contract with the National Aeronautics and Space Administration under the Exoplanet Exploration Program. This work makes use of observations made with the ESO 3.6 m telescope at the European Southern Observatory (ESO), La Silla, under ESO programmes 1102.C-0923, 0102.C-0338, 0103.C-0442, 0103.C-0548, 60.A-9700 and 60.A-9709. We are very grateful to the ESO staff members for their precious support during the observations. We warmly thank X. Dumusque and F. Bouchy for coordinating the shared observations with HARPS and J. Alvarado Montes, X. Delfosse, G. Gaisné, M. Hobson and D. Barrado Navascués, who helped collecting the HARPS spectra. This work has made use of data from the European Space Agency mission Gaia (https://www.cosmos.esa.int/gaia), processed by the Gaia Data Processing and Analysis Consortium (https://www.cosmos.esa.int/web/gaia/dpac/consortium). Funding for the Data Processing and Analysis Consortium has been provided by national institutions, in particular the institutions participating in the Gaia Multilateral Agreement. This work makes use of observations from the LCOGT network. LCOGT telescope time was granted by NOIRLab through the Mid-Scale Innovations Program, which is funded by the National Science Foundation. Some of the observations in the paper made use of the high-resolution imaging instrument Zorro. Zorro was funded by the NASA Exoplanet Exploration Program and built at the NASA Ames Research Center by S. B. Howell, N. Scott, E. P. Horch and E. Quigley. Data was reduced using a software pipeline originally written by E. Horch and M. Everett. Zorro was mounted on the Gemini South telescope and the Near Infrared Imager (NIRI) was mounted on the Gemini North telescope, of the international Gemini Observatory, a programme of the National Science Foundation's OIR Lab, which is managed by the Association of Universities for Research in Astronomy under a cooperative agreement with the National Science Foundation on behalf of the Gemini partnership: the National Science Foundation (United States), National Research Council (Canada), Agencia Nacional de Investigación y Desarrollo (Chile), Ministerio de Ciencia, Tecnología e Innovación (Argentina), Ministério da Ciência, Tecnologia, Inovações e Comunicações (Brazil) and Korea Astronomy and Space Science Institute (Republic of Korea). Data collected under programme GN-2019A-LP-101. This work was based in part on observations obtained at the SOAR telescope, which is a joint project of the Ministério da Ciência, Tecnologia e Inovações do Brasil, the US National Science Foundation's NOIRLab, the University of North Carolina at Chapel Hill and Michigan State University. This research has made use of the NASA Exoplanet Archive, which is operated by the California Institute of Technology, under contract with the National Aeronautics and Space Administration under the Exoplanet Exploration Program. L.M.S. and D.G. gratefully acknowledge financial support from the CRT foundation under Grant No. 2018.2323 "Gaseous or rocky? Unveiling the nature of small worlds." E.Gu. acknowledges the generous support by the Thüringer Ministerium für Wirtschaft, Wissenschaft und Digitale Gesellschaft. I.G., C.M.P., M.Fr. and A.J.M. gratefully acknowledge the support of the Swedish National Space Agency (DNR 174/18, 65/19, 120/19C). J.K. gratefully acknowledges the support of the Swedish National Space Agency (DNR 2020-00104). S.C., M.E., K.W.F.L., S.G. and A.P.H. acknowledge support by DFG grants RA714/14-1 within the DFG Schwerpunkt SPP 1992, "Exploring the Diversity of Extrasolar Planets". M.R.D. acknowledges the support by Comisión Nacional de Investigación Científica y Tecnológica (CONICYT)-PFCHA/Doctorado Nacional-21140646, Chile. T.D. acknowledges support from MIT's Kavli Institute as Kavli postdoctoral fellow. T.T. acknowledges support by the DFG Research Unit FOR 2544 "Blue Planets around Red Stars" project No. KU 3625/2-1. T.T. further acknowledges support by the BNSF programme "VIHREN-2021" project No. КП-06-ДВ/5.

Author contributions

L.M.S. performed the periodogram analysis and the joint analysis with pyaneti, wrote most of the text and coordinated the contributions from the other co-authors. D.G. performed the radial velocity analysis using the floating chunk offset method, wrote a significant part of the text and is the principal investigator of the HARPS large programme, which enabled the discovery of three additional planets and the determinations of the planetary (minimum) masses. O.B. performed the multi-dimensional Gaussian process analysis and wrote the relative section. J.K. ran the stability analyses with rebound and SPOCK and wrote the relative section. A.J.M. and F.D. described the most probable formation/migration processes of the system. A.J.M. also ran the numerical simulation to test the low-eccentricity migration pathway and wrote the relative section. M. Fridlund performed the spectral and chemical abundance analysis. K.W.F.L. and S.G. searched the TESS light curve for transit signals. K.A.C. performed the LCOGT observations and analysed the data. J.H.L. analysed the GEMINI and SOAR imaging data. J.A., M.R.D., F.R. and T.T. contributed to the HARPS RV follow-up. W.D.C. computed the probability that TOI-500 belongs to different stellar populations. C.H. analysed the WASP-South light curves. S.E.B. contributed to the analysis of the radial velocity data. S.R. explored the possibility to study the secondary atmosphere of TOI-550 b and wrote the relative section. S.A., S.C., H.J.D., M.E., I.G., E. Goffo, E. Guenther, A.P.H., R.L., F.M., H.L.M.O., E.P., C.M.P., A.M.S.S. and V.V.E. are members of the KESPRINT consortium and contributed to the HARPS large programme. C.Z. and A.W.M. performed the SOAR imaging observations. E.L.N.J. contributed to the LCOGT observations. S.B.H. performed the observations with GEMINI/ZORRO. J.M.J., D.W.L., G.R., S.S., R.V. and J.N.W. are the architects of the TESS mission. K.I.C., T.D., M. Fasnaugh, A.W.M., P.R., A.R. and J.D.T. significantly contributed to the success of the TESS mission, which discovered the USP planet candidate. All authors reviewed the manuscript.

Competing interests

The authors declare no competing interests.

Additional information

Extended data is available for this paper at https://doi.org/10.1038/s41550-022-01641-y.

Supplementary information The online version contains supplementary material available at https://doi.org/10.1038/s41550-022-01641-y.

Correspondence and requests for materials should be addressed to Luisa Maria Serrano.

Peer review information *Nature Astronomy* thanks the anonymous reviewers for their contribution to the peer review of this work.

Reprints and permissions information is available at www.nature.com/reprints.

Publisher's note Springer Nature remains neutral with regard to jurisdictional claims in published maps and institutional affiliations.

[1]Dipartimento di Fisica, Università degli Studi di Torino, Turin, Italy. [2]Lund Observatory, Department of Astronomy and Theoretical Physics, Lund University, Lund, Sweden. [3]Sub-department of Astrophysics, Department of Physics, University of Oxford, Oxford, UK. [4]Department of Space, Earth and Environment, Astronomy and Plasma Physics, Chalmers University of Technology, Gothenburg, Sweden. [5]Division of Geological and Planetary Sciences, Pasadena, CA, USA. [6]Astronomy Department and Van Vleck Observatory, Wesleyan University, Middletown, CT, USA. [7]Leiden Observatory, Leiden University, Leiden, the Netherlands. [8]Department of Space, Earth and Environment, Chalmers University of Technology, Onsala Space Observatory, Onsala, Sweden. [9]Center for Astronomy and Astrophysics, TU Berlin, Berlin, Germany. [10]Departamento de Astronomía, Universidad de Chile, Santiago, Chile. [11]Las Campanas Observatory, Carnegie Institution of Washington, La Serena, Chile. [12]Rheinisches Institut für Umweltforschung an der Universität zu Köln, Cologne, Germany. [13]Center for Astrophysics | Harvard & Smithsonian, Cambridge, MA, USA. [14]Department of Astronomy, University of Tokyo, Tokyo, Japan. [15]Department of Astronomy and McDonald Observatory, University of Texas at Austin, Austin, TX, USA. [16]Astrophysics Group, Keele University, Staffordshire, UK. [17]Max Planck Institut für Astronomie, Heidelberg, Germany. [18]Department of Astronomy, Faculty of Physics, University of Sofia, Sofia, Bulgaria. [19]European Southern Observatory, Santiago de Chile, Chile. [20]NASA Ames Research Center, Moffett Field, CA, USA. [21]Harvard–Smithsonian Center for Astrophysics, Cambridge, MA, USA. [22]Department of Physics and Kavli Institute for Astrophysics and Space Research, Massachusetts Institute of Technology, Cambridge, MA, USA. [23]Department of Earth, Atmospheric and Planetary Sciences, Massachusetts Institute of Technology, Cambridge, MA, USA. [24]Department of Aeronautics and Astronautics, MIT, Cambridge, MA, USA. [25]Department of Astrophysical Sciences, Princeton University, Princeton, NJ, USA. [26]Stellar Astrophysics Centre, Department of Physics and Astronomy, Aarhus University, Midtbyen, Denmark. [27]George Mason University, Fairfax, VA, USA. [28]Institute of Planetary Research, German Aerospace Center (DLR), Berlin, Germany. [29]Instituto de Astrofísica de Canarias (IAC), La Laguna, Spain. [30]Departamento de Astrofísica, Universidad de La Laguna (ULL), La Laguna, Spain. [31]Thüringer Landessternwarte Tautenburg, Tautenburg, Germany. [32]Department of Physics & Astronomy, Swarthmore College, Swarthmore, PA, USA. [33]Department of Physics and Astronomy, The University of North Carolina at Chapel Hill, Chapel Hill, NC, USA. [34]Mullard Space Science Laboratory, University College London, Dorking, UK. [35]Royal Astronomical Society, London, UK. [36]Institute for Planetary Research, German Aerospace Center (DLR), Berlin, Germany. [37]SETI Institute, Mountain View, CA, USA. [38]Department of Physics, Engineering and Astronomy, Stephen F. Austin State University, Nacogdoches, TX, USA.
✉e-mail: luisamaria.serrano@unito.it

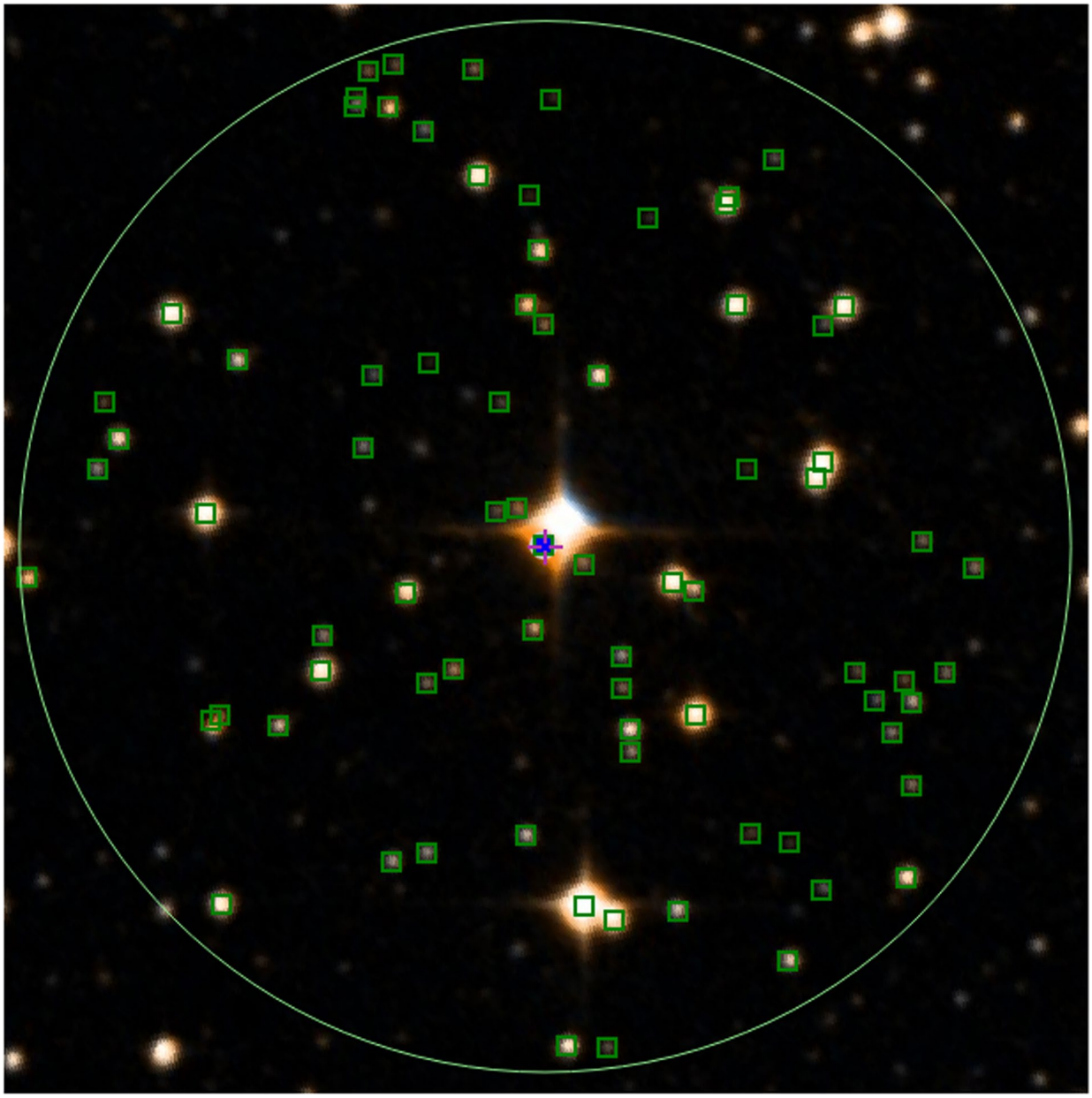

Extended Data Fig. 1 | Field of view with the locations of the 78 *Gaia* DR2 stars checked for NEBs. The circle marks a 2.5′radius around TOI-500. The background image is from the digitized sky survey 2 (DSS2). The circles on each star represent the current Gaia DR2 position. The different timing between the DSS2 and DR2 databases is the reason for which some of the stars are shifted from the original position, as a consequence of their proper motion.

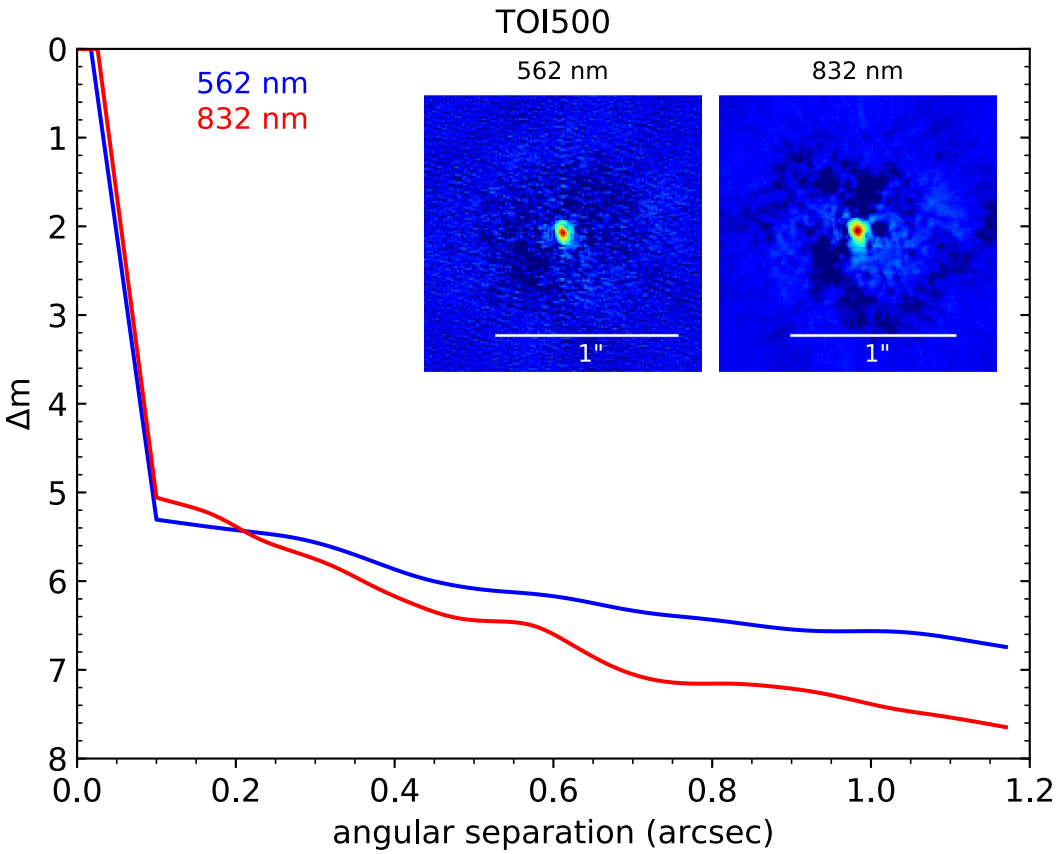

Extended Data Fig. 2 | Gemini/Zorro 5-sigma contrast curve. and 1.2″ × 1.2″ reconstructed images (inset).

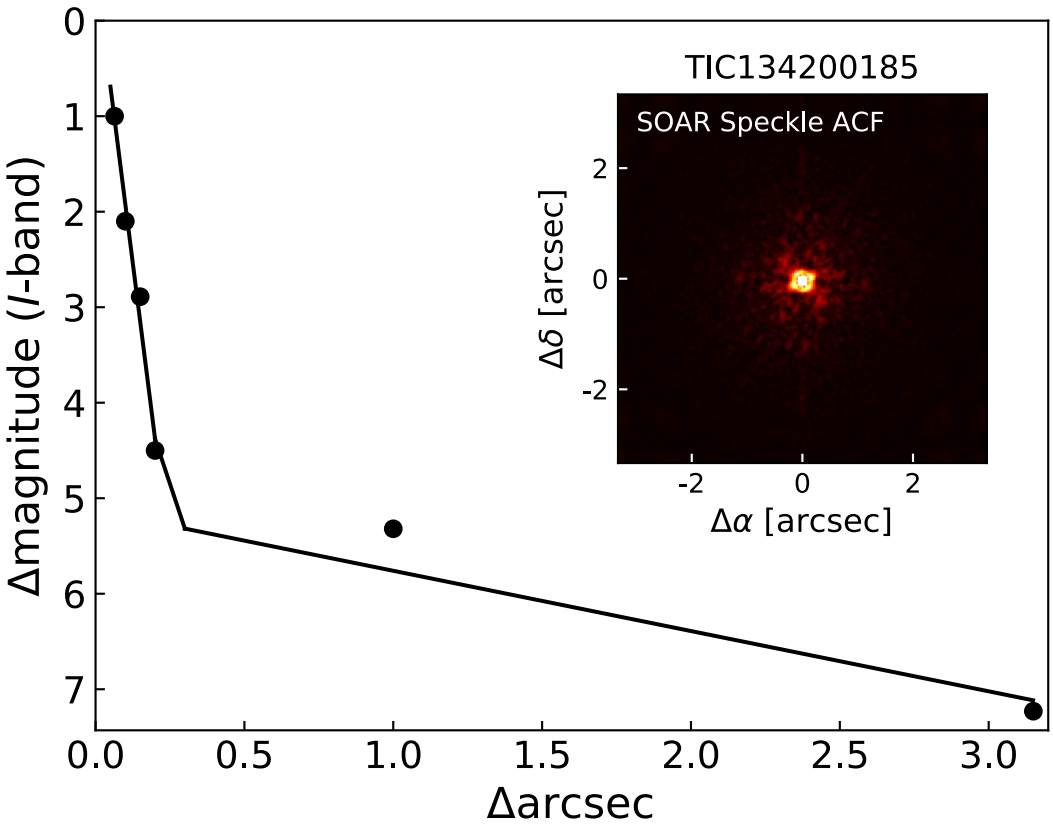

Extended Data Fig. 3 | *SOAR* contrast curve. and 6″×6″ two-dimensional auto-correlation function of *SOAR* image (inset).

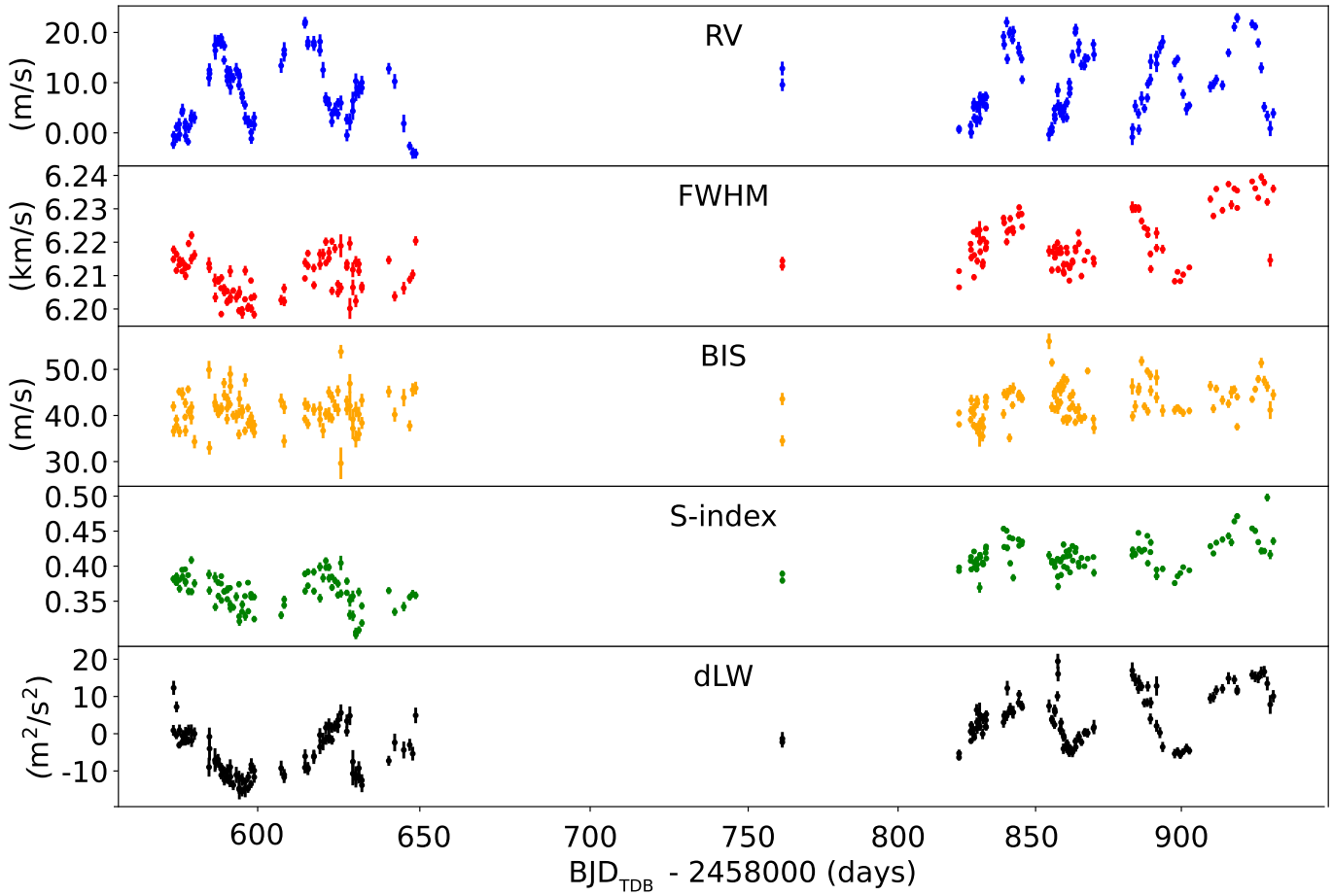

Extended Data Fig. 4 | Time series of the *HARPS* RV measurements. and activity indicators (FWHM, BIS, S-index, and dLW).

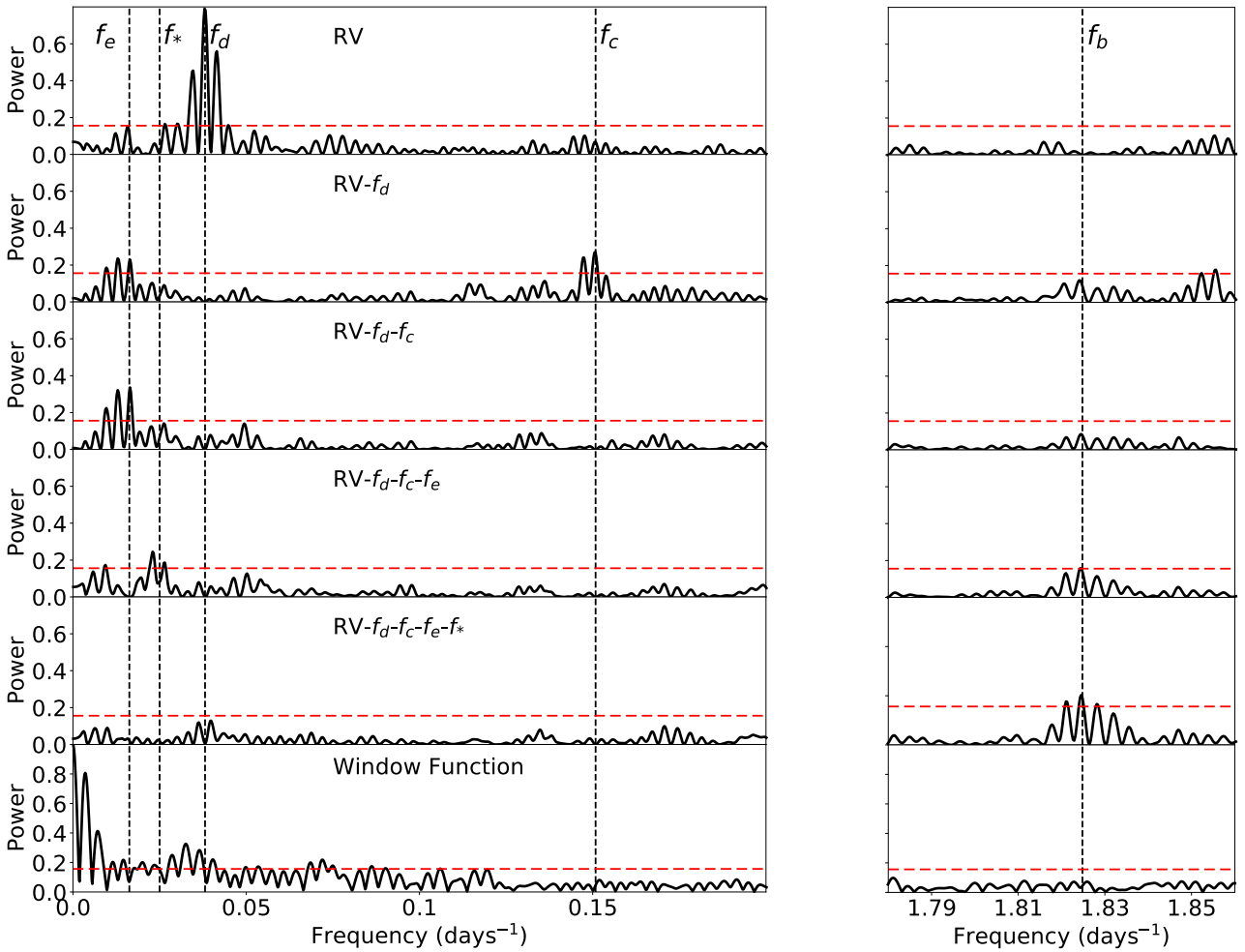

Extended Data Fig. 5 | Generalized Lomb-Scargle periodograms of the *HARPS* SERVAL RV measurements and residuals. The right and left columns cover two frequency ranges encompassing the Doppler signals of TOI-500 c, d, e, and the stellar rotation frequency f* (*left panels*), and the orbital frequency of the USP planet TOI-500 b (*right panels*). From top to bottom: RV data (*upper panel*); RV residuals following the subtraction of the Doppler signal of TOI-500 d (*second panel*), TOI-500 d and c (*third panel*), TOI-500 d, c, and e (*fourth panel*), TOI-500 d, c, and e plus the stellar signal at 43.4 d (*fifth panel*); window function (*lower panel*). The red dashed horizontal lines mark the 0.1 % false alarm probability as derived using the bootstrap method. The vertical dashed lines mark the significant frequencies identified in the *HARPS* data and discussed in the main text.

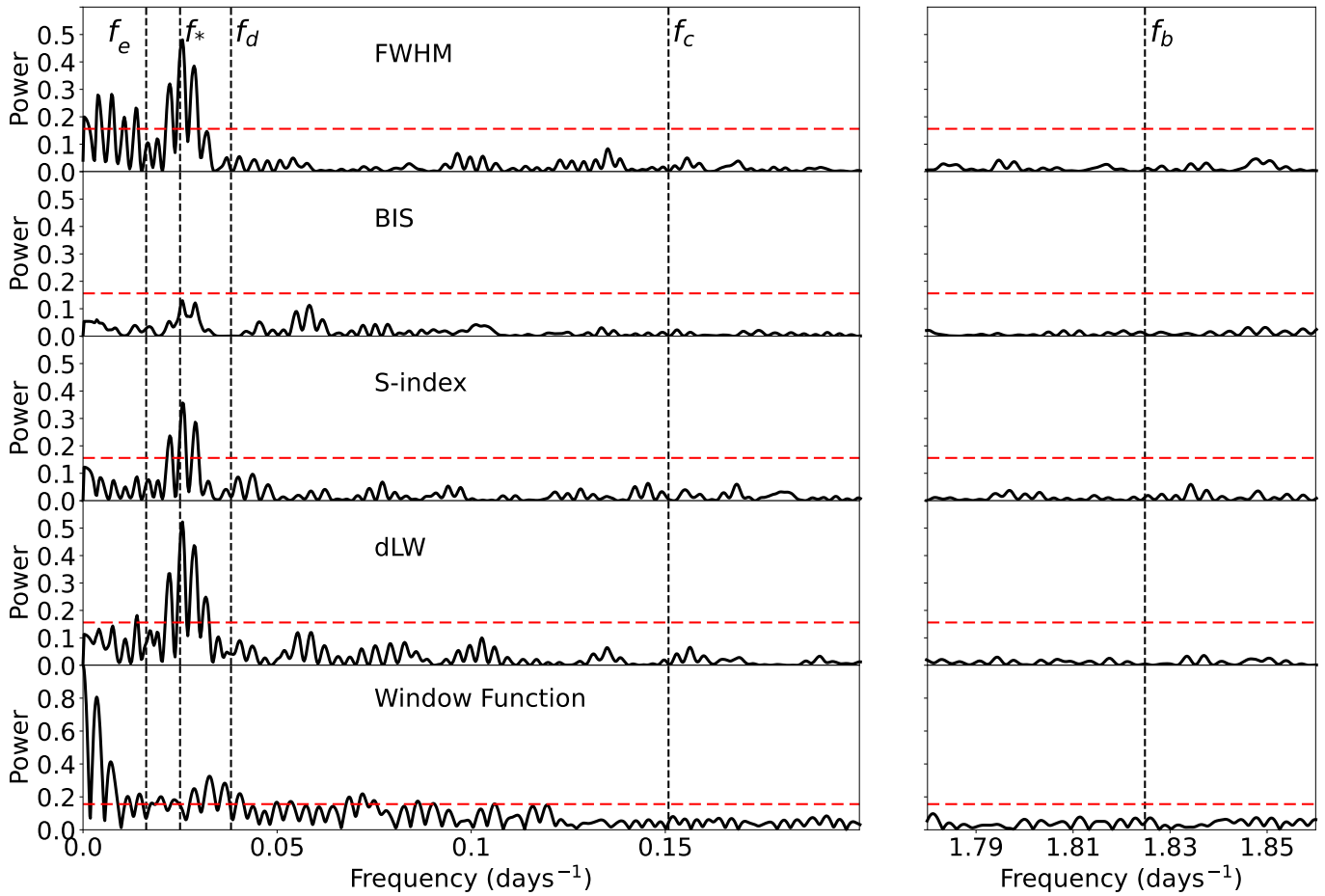

Extended Data Fig. 6 | Generalized Lomb-Scargle periodograms of the activity indicators following the subtraction of the seasonal median values (see Methods). The right and left columns cover two frequency ranges encompassing the Doppler signals induced by the 4 orbiting planets and stellar rotation. From top to bottom: FWHM (*upper panel*), BIS (*second panel*), S-index (*third panel*), dLW (*fourth panel*), window function (*lower panel*). The red dashed horizontal lines mark the 0.1% false alarm probability as derived using the bootstrap method. The vertical dashed lines mark the significant frequencies identified in the *HARPS* data and discussed in the main text.

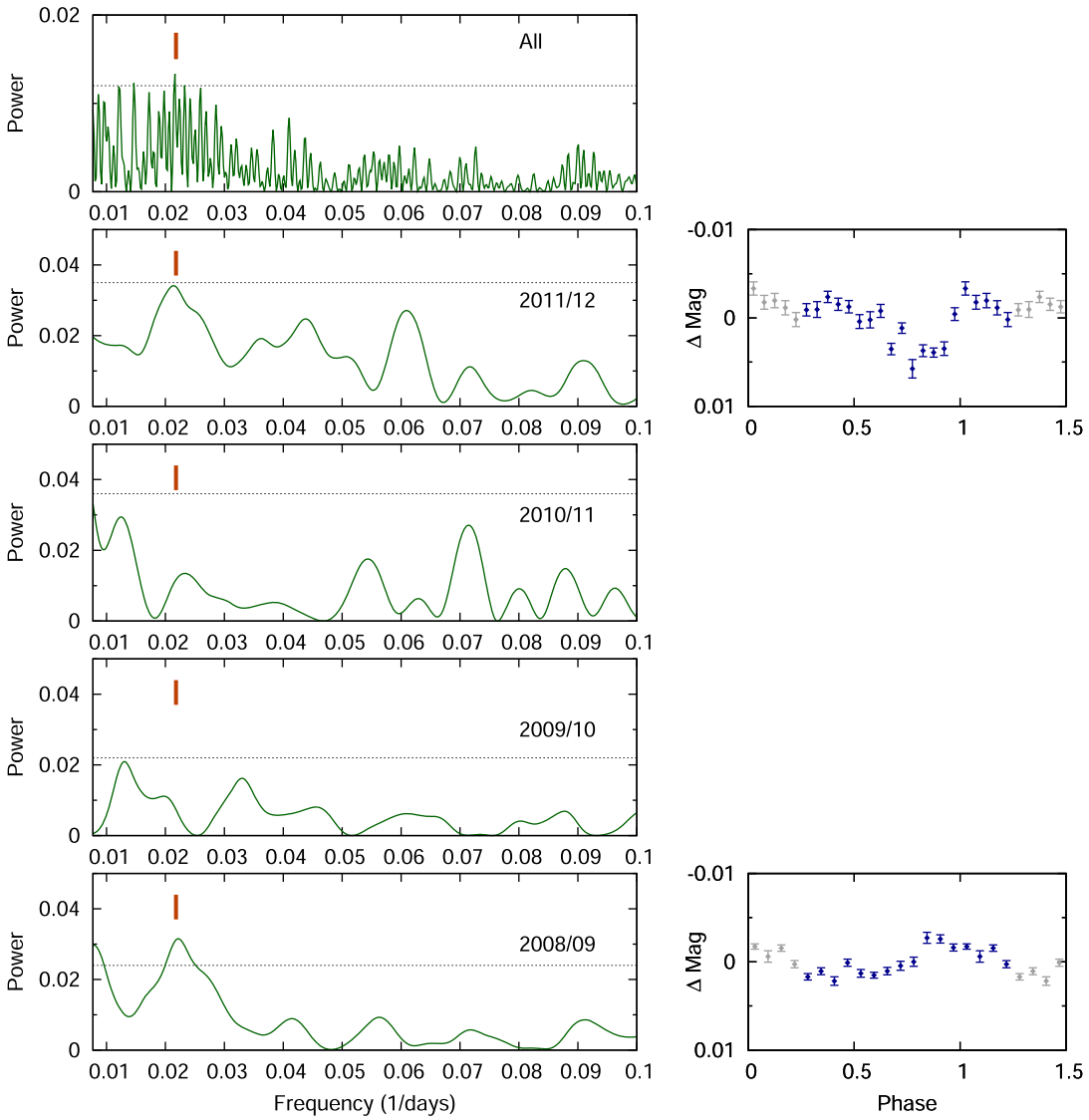

Extended Data Fig. 7 | Lomb-Scargle periodograms of the *WASP-South* light curves of TOI-500. *Left panels, from bottom to top*: periodogram of the data acquired in 2008/2009, 2009/2010, 2010/2011, and 2011/2012. The *upper left panel* displays the periodogram of the combined 4 years of data, showing a possible 0.022d-1 periodic signal, corresponding to a period of about 45 d (*upper panel*). This peak is marked in all the panels with a red thick line. The dotted horizontal lines show the 1% false alarm probability. The *right panels* show the *WASP-South* binned photometry folded at the 45-d rotation period for the years 2008 and 2011, when the 45 d signal is stronger. The displayed phases go from 0 to 1.5, in order to visualize better the periodicity of the photometric variability. The repeated data between phase 0 and 0.25, and phase 1.25 and 1.5 are shown with gray points.

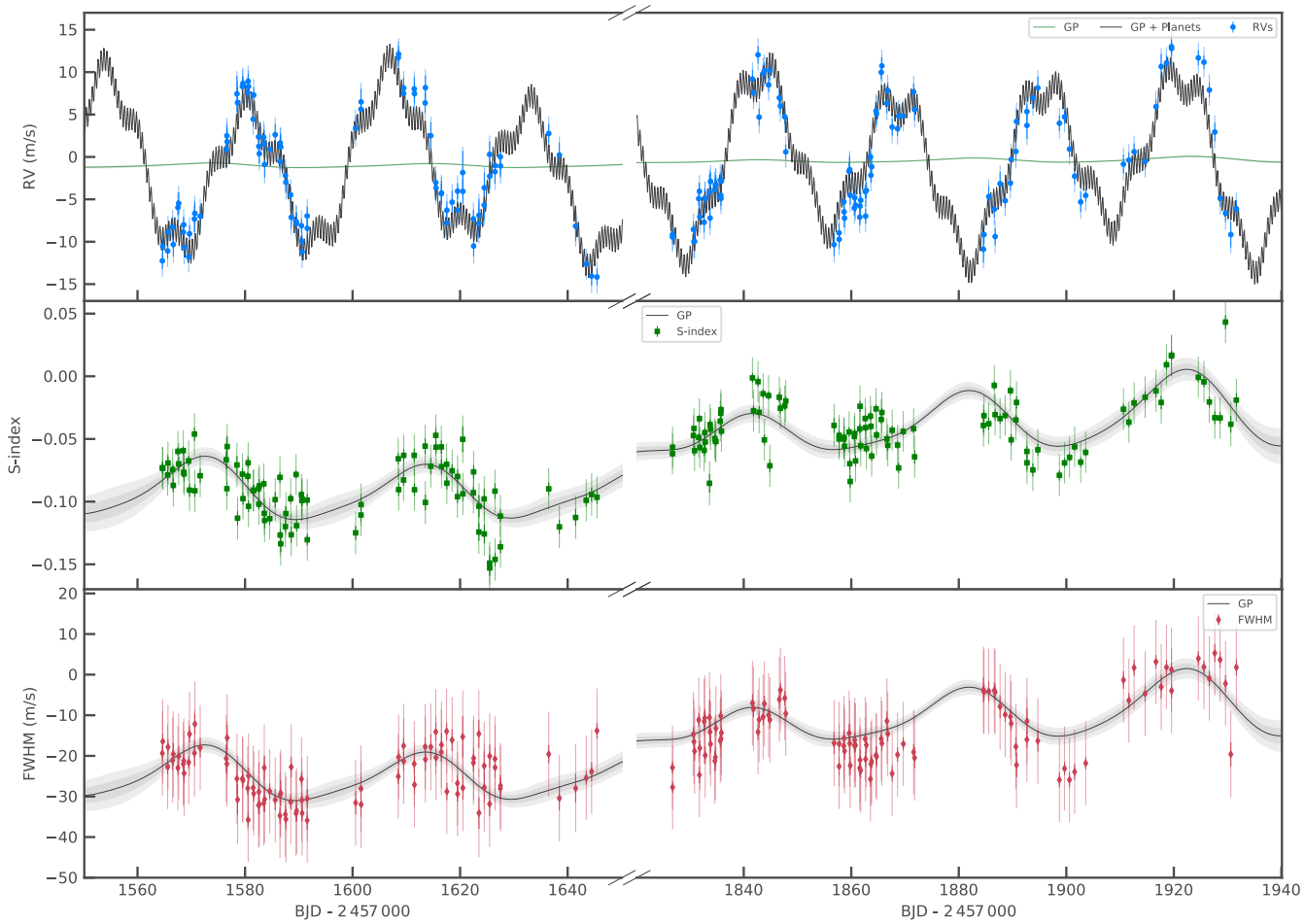

Extended Data Fig. 8 | Median-subtracted *HARPS* SERVAL RVs (*upper panel*), S-index (*middle panel*), and FWHM (*lower panel*). *Upper panel: HARPS* SERVAL RVs (blue data points), GP model (green line), and best fitting (GP+planets) model (thick black line). *Middle panel*: S-index (green data points) and GP model (thick black line). Lower panel: FWHM (red data points) and GP model (thick black line). Nominal error bars are shown in solid colour, and the error bars corrected by jitter are semitransparent. Dark and light shaded areas show the 1- and 2- σ confidence interval of the corresponding GP model, respectively. We note that there is a gap between 1650 and 1820 BJD - 2457000$d.

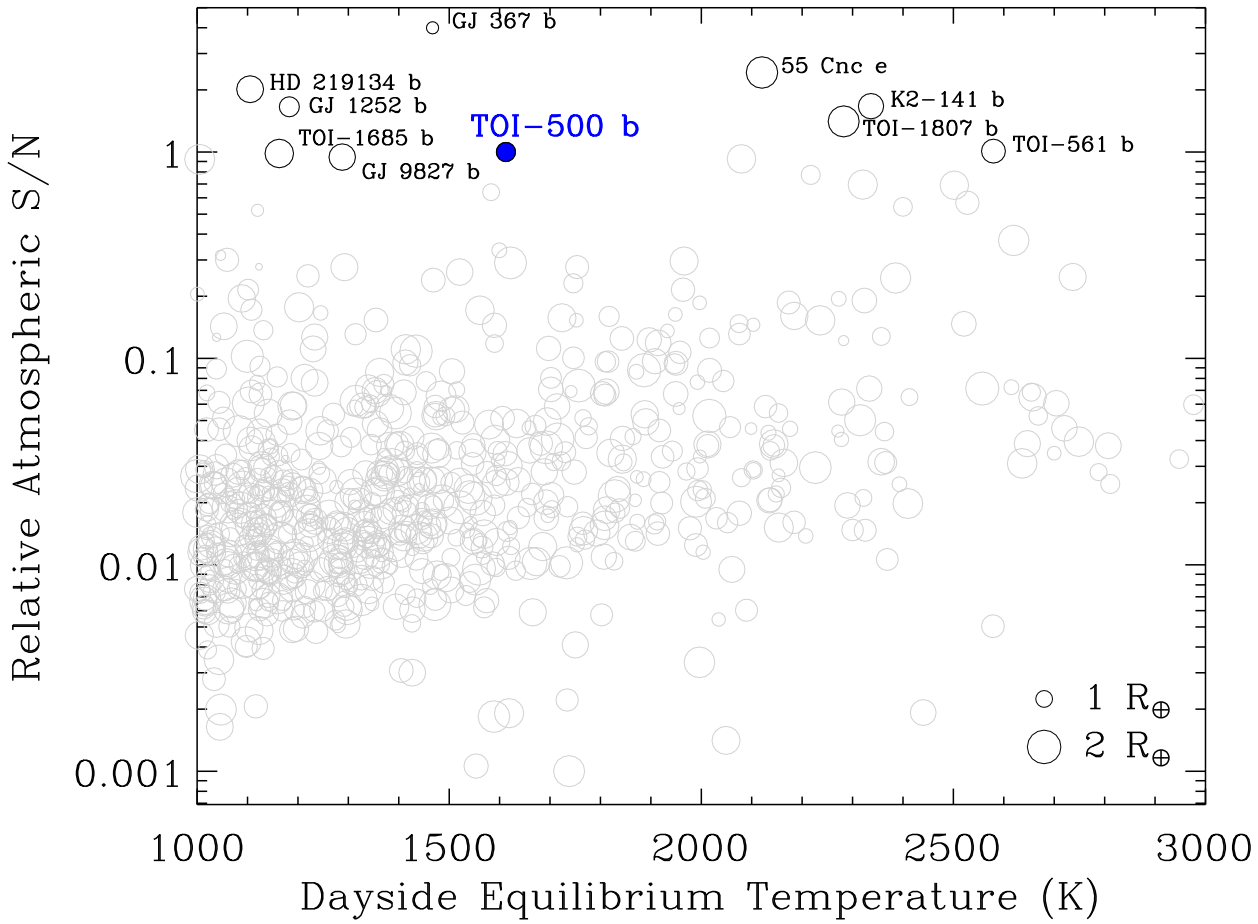

Extended Data Fig. 9 | Scatter plot of exoplanets with atmospheric S/N ratio. as a function of the dayside predicted equilibrium temperature in Kelvin. TOI-500b is in a favorable position among the top 10 targets of interest for atmospheric characterization.